Title: Inflammation-induced alteration of astrocyte mitochondrial dynamics requires autophagy for mitochondrial network maintenance.
Authors: Motori E, Puyal J, Toni N, Ghanem A, Angeloni C, Malaguti M, Cantelli-Forti G, Berninger B, Conzelmann KK, Götz M, Winklhofer KF, Hrelia S, Bergami M
Journal: Cell metabolism
Year: 2013 Dec 3
Volume: 18
Issue: 6
Pages: 844-59
DOI: 10.1016/j.cmet.2013.11.005

Inflammation-induced alteration of astrocyte mitochondrial dynamics requires autophagy for mitochondrial network maintenance

Elisa Motori[1,*], Julien Puyal[2], Nicolas Toni[2], Alexander Ghanem[3], Cristina Angeloni[1], Marco Malaguti[1], Giorgio Cantelli-Forti[1], Benedikt Berninger[4,5,6], Karl-Klaus Conzelmann[3], Magdalena Götz[4,7,8], Konstanze F. Winklhofer[8,9,10,11], Silvana Hrelia[1,13] and Matteo Bergami[4,12,13,*]

[1] Department for Life Quality Studies - Alma Mater Studiorum, University of Bologna, via Irnerio 48, 40126 Bologna, Italy;

[2] Department of fundamental Neurosciences, University of Lausanne, 9 rue du Bugnon, 1005 Lausanne, Switzerland;

[3] Max von Pettenkofer Institute and Gene Center, Ludwig Maximilians-University Munich, Germany;

[4] Physiological Genomics, Institute of Physiology, Ludwig Maximilians University Munich, Schillerstrasse 46, D-80336 Munich, Germany;

[5] Institute of Physiological Chemistry, University Medical Center of the Johannes Gutenberg University, D-55128 Mainz, Germany;

[6] Focus Program Translational Neuroscience, Johannes Gutenberg University, Mainz, Germany;

[7] Institute of Stem Cell Research, Helmholtz Zentrum München, Ingolstädter Landstrasse 1, D-85764 Neuherberg, Germany;

[8] Munich Cluster for Systems Neurology (SyNergy), Schillerstrasse 44, D-80336, Munich, Germany;

[9] Adolf Butenandt Institute, Neurobiochemistry, Ludwig Maximilians University Munich, Schillerstrasse 44, D-80336 Munich, Germany;

[10] German Center for Neurodegenerative Diseases (DZNE) Schillerstrasse 44, D-80336 Munich, Germany;

[11] Molecular Cell Biology, Institute of Physiological Chemistry, Ruhr University Bochum, Universitaetsstrasse 150, D-44801 Bochum, Germany;

[12] Cologne Excellence Cluster on Cellular Stress Responses in Aging-Associated Diseases (CECAD), University of Cologne, Zuelpicher Strasse 47a, D-50674 Cologne, Germany;

[13] These authors contributed equally;

[*] Correspondence: Elisa Motori

Department for Life Quality Studies,

University of Bologna, Italy

Email: elisa.motori@unibo.it

Matteo Bergami

CECAD-University of Cologne, Germany

Email: matteo.bergami@uk-koeln.de

Elisa Motori's presents address: Max Planck Institute for Biology of Ageing, Cologne, Germany.

Running title: Mitochondrial dynamics in reactive astrocytes

Summary

Accumulating evidence suggests that changes in the metabolic signature of astrocytes underlie their response to neuroinflammation, but how pro-inflammatory stimuli are transduced into these changes is poorly understood. By monitoring mitochondrial dynamics in astrocytes following cortical injury and the ensuing inflammation, we identified a differential and region-specific remodelling of their mitochondrial network: while astrocytes within the penumbra of the lesion undergo elongation of mitochondria, those located in the lesion core - the area invaded by pro-inflammatory cells - experience transient mitochondrial fragmentation. In brain slices, focal pro-inflammatory stimulation reproduced localized changes in mitochondrial dynamics favouring fission over fusion, thus leading to fragmentation. This effect was triggered by Drp1 phosphorylation and ultimately resulted in reduced respiratory capacity. Furthermore, maintenance of the mitochondrial architecture critically depended on the induction of autophagy. Deletion of *Atg7*, required for autophagosome formation, prevented the re-establishment of tubular mitochondria, leading to marked ROS accumulation and cell death. Thus, our data reveal autophagy to be essential for regenerating astrocyte mitochondrial networks during inflammation.

Introduction

By virtue of their strategic position, astrocytes sustain brain tissue homeostasis and critically contribute to synaptic function by locally interacting with neurons and the vasculature (Halassa et al., 2007; Iadecola and Nedergaard, 2007). In many neuropathologies characterized by a strong inflammatory component, including traumatic brain injury, ischemia and chronic neurodegeneration, astrocytes enter a highly reactive state (Sofroniew, 2009) suggested to contribute to ameliorating or worsening the pathology (Bush et al., 1999; Menet et al., 2003; Okada et al., 2006). Recently, whole-cell transcriptome analysis of astrocytes exposed to pro-inflammatory insults revealed the transient up-regulation of important and stimulus-specific metabolic pathways (Hamby et al., 2012; Zamanian et al., 2012), strongly arguing for their active role in the energy metabolism of the diseased brain (Belanger et al., 2011a; Farina et al., 2007; Sofroniew, 2009).

Although astrocytes can remarkably increase their glycolytic and glycogenolytic metabolism in response to neuronal activity (Belanger et al., 2011a; Hertz et al., 2007; Kasischke et al., 2004), their energy production is largely based on mitochondrial oxidative metabolism (Hertz et al., 2007). Supporting this notion, abundant mitochondria have been observed within the finest astrocytic processes *in vivo* (Lovatt et al., 2007; Mathiisen et al., 2010), speaking in favour of the important role of mitochondria in energy supply and metabolic signalling in astroglial cells. The mitochondrial network in most mammalian cells is normally composed of tubular mitochondria whose shape and dynamics are continuously remodelled by opposing fusion and fission reactions. The central players in catalyzing these reactions are several conserved GTP-binding proteins that execute specifically either mitochondrial fusion (e.g. mitofusin 1 and 2; optic atrophy 1, OPA1) or fission (dynamin-related protein, Drp1; and fission 1 protein, Fis1) (Liesa et al., 2009). While on one side the

proper balance between these reactions is key for preserving mitochondrial architecture and metabolism (i.e., respiratory capacity and energy production), on the other side it ensures appropriate distribution of mitochondrial DNA and other mitochondrial components (Liesa et al., 2009). Failure to properly regulate mitochondrial dynamics may lead to damaged mitochondria, a condition associated with aging and several neurodegenerative diseases (Detmer and Chan, 2007; Knott et al., 2008).

Given the peculiar cellular distribution of mitochondria in astrocytes and their key role in energy metabolism, it is reasonable to assume that they may directly participate in the metabolic changes associated with astrogliosis and neuroinflammation. Intriguingly, astrocytes reacting to inflammatory stimuli *in vitro* significantly increase their rate of glycolysis, rather than oxidative phosphorylation, to prevent ATP depletion and cell death (Almeida et al., 2001; Almeida et al., 2004; Brown et al., 1995), thus raising the question whether mitochondrial function becomes altered during inflammation. Interestingly, one of the suggested mechanisms responsible for the quality control of mitochondria is mitophagy, a specific form of macroautophagy aimed at regulating mitochondrial turn-over and possibly at segregating damaged mitochondria from the healthy network (Wang and Klionsky, 2011). Whether autophagy plays any role in coordinating mitochondrial network function in reactive astrocytes is not known.

In this study, we show that astrocytes *in vivo* and *in vitro* respond to pro-inflammatory stimuli with a remarkably regionalized - albeit transient - change of their mitochondrial dynamics favouring fission over fusion. We provide compelling evidence that Drp1 is the enzyme required for the observed mitochondrial fragmentation. Finally, we show that this transient phase of mitochondrial alteration is accompanied by a marked increase in ROS production and autophagy, the latter

required for restoring tubular mitochondria and sustaining cell survival at later time points. Thus, our results reveal that a timely activation of autophagy is critical to safeguard mitochondrial function in astrocytes during a pro-inflammatory response.

Results

Acute cortical injury induces differential and region specific remodelling of astrocyte mitochondrial networks

To label mitochondria selectively in astrocytes *in vivo* we took advantage of a mouse line expressing the avian *TVA* receptor for the envelope glycoprotein EnvA under the control of the human glial fibrillary acidic protein promoter (hGFAP-*TVA* mice) (Holland and Varmus, 1998). In these mice, intra-cortical delivery of an EnvA-pseudotyped rabies virus (Wickersham et al., 2007b) encoding for mitochondrially-targeted *GFP* (*mito-GFP*) (referred as to mito-RABV; **Figure 1A**) resulted in the efficient labelling of mitochondria specifically in astrocytes (**Figure 1B-1C and Figure S1A-S1E**). Interestingly, astrocytes displayed a fine network of tubular mitochondria reaching the most peripheral cellular processes (**Figure S1E**), often found in close proximity to nearby neurons (**Figure S2**).

We then examined mitochondrial networks in astrocytes following cortical stab wound (SW) (Bardehle et al., 2013), a well established paradigm of acute injury which results in the activation of glial cells within the injured area, local neuroinflammation and scar formation (Sofroniew, 2009). Combined delivery of mito-RABV with SW led to efficient targeting of *mito-GFP* to astrocytes localized in the injured area (**Figure 1D-1E**). Interestingly, while astrocytes in control uninjured hemispheres displayed a mostly tubular mitochondrial network (**Figure 1F**), by 4 days post-injection (dpi) astrocytes in the lesioned site could be classified into two

distinct categories depending on their location and morphology of their mitochondria (**Figure 1E-1F**). Astrocytes located in the penumbra of the lesion, i.e., the scar forming region (S100β+/GFAP+ astrocytes), displayed hypertrophic and polarized processes (Bardehle et al., 2013; Wilhelmsson et al., 2006) and their mitochondria appeared as an interconnected meshwork of elongated organelles (**Figure 1F**). In contrast, astrocytes within the lesion core were devoid of GFAP immunoreactivity and their mitochondria were characterized by a prominent fragmented/rod-like shape (**Figure 1F**). The majority of these astrocytes were neither in mitosis or apoptotic, as their nuclei appeared uniform and no signs of pyknosis were detectable (**Figure 1F and Figure S3C**). Time-course analysis of lesion core astrocytes revealed a drastic reduction in their mitochondrial length compared to astrocytes of non-lesioned hemispheres at 2 and 4dpi (**Figure 1G-1H**). Notably, by 10dpi their mitochondrial length had returned to similar levels as that of control astrocytes (**Figure 1G-1H**), suggesting extensive but transient changes in their mitochondrial dynamics toward fission (Detmer and Chan, 2007; Youle and van der Bliek, 2012). On the other hand, astrocytes in the penumbra (S100β+/GFAP+) never exhibited massive fragmentation and showed an opposite dynamic reorganization of their mitochondrial networks (**Figure 1H and Figure S3C**), which matched in time with the acquisition of typical traits of gliosis (Bardehle et al., 2013; Sofroniew, 2009; Wilhelmsson et al., 2006; Zamanian et al., 2012). Interestingly, in these astrocytes the mitochondrial response occurred delayed compared to the lesion core and displayed high levels of elongation up to 10dpi (**Figure 1H**). Together, these data demonstrate that marked but opposite changes in mitochondrial dynamics characterize astrocytes within the lesion core compared to those in the penumbra.

Focal infusion of IL-1β induces local changes in the mitochondrial dynamics of astrocytes in acute brain slices

A major stimulus triggering astrocyte reactivity within the immediate lesion area is the local release of pro-inflammatory cytokines from inflammatory cells (Hamby et al., 2012; Sofroniew, 2009; Zamanian et al., 2012). Indeed, pro-inflammatory cells including locally recruited Iba1+ microglia and infiltrating blood-derived CD45+ leukocytes were greatly enriched in the lesion core (**Figure 2A-2B, S3A and S4A**). Accordingly, this region appeared highly immunoreactive for IL-1β (**Figure 2C**), one of the major pro-inflammatory cytokines released following trauma (Pinteaux et al., 2009). This prompted us to investigate whether the unique mitochondrial rearrangements observed in astrocytes within the lesion core could be attributed to the local pro-inflammatory microenvironment consequent to SW. We thus prepared acute slices from uninjured, mito-RABV injected mice and analyzed mitochondrial dynamics, i.e., fission and fusion, in astrocytes under focal application of IL-1β by time-lapse confocal microscopy (**Figure 2D-2F**). By 30 minutes following IL-1β treatment, we observed a conspicuous increment in mitochondrial fission (70-80% of all events) in astrocyte branches proximal to the pipette (for simplicity defined as quadrant I, i.e., the astrocyte branches within the diffusion radius of the cytokine; **Figure S4B-S4C**), in which initially tubular mitochondria appeared to fragment over time (**Figure 2G-2I**), however without overtly affecting astrocyte integrity (**Figure S4D-S4F**). In sharp contrast, more distal regions of the astrocytes did not exhibit any increase in fission events but rather slightly increased mitochondrial fusion (**Figure 2H-2I**), ultimately contributing to balance the overall proportion of fission and fusion events (**Figure 2I**, black line). Different from these dynamics, infusion of ACSF alone did not induce significant alterations of the mitochondrial network (**Figure 2K-2L**). These results suggest that, within the physiological context of a brain slice,

astrocytes rapidly react to pro-inflammatory stimuli by locally increasing mitochondrial fission.

Pro-inflammatory stimuli alter mitochondrial morphology and dynamics in cultured astrocytes

To understand the molecular mechanism underlying the changes in mitochondrial networks in astrocytes exposed to pro-inflammatory insults, we analyzed primary cortical astrocytes in culture (**Figure 3A**) following direct stimulation with LPS+IFNγ, a well established combination of factors used to mimic *in vitro* the inflammatory response (Brown et al., 1995; Hamby et al., 2012). Time-course analysis of mitochondrial morphology revealed a progressive rearrangement of the network resulting in the generation of rod-like structures starting from 1h after treatment, followed by extensive mitochondrial fragmentation at 4-8h later (**Figure 3B**). Accordingly, mitochondrial length in stimulated astrocytes significantly decreased at 4 and 8h after treatment (**Figure 3C-3D**). In marked contrast, by 24h mitochondria displayed a tubular morphology similar to that of untreated control cells (**Figure 3B-3D**). A similar reduction in mitochondrial length compared to controls was obtained following treatment with other pro-inflammatory cytokines (IL-1β, IL-6 and TNF-α; **Figure S5A**), the up-regulation of which has been detected following brain trauma (Bethea et al., 1999; Kamm et al., 2006), suggesting that mitochondria are a common downstream target of the inflammatory signalling pathway in astrocytes. Consistent with previous studies (Bardehle et al., 2013; Brown et al., 1995; Stewart et al., 1998), pro-inflammatory stimuli did not alter astrocyte viability within the examined time window (**Figure S5B-S5C**).

To gain further insights into the mitochondrial reorganization observed in LPS+IFNγ stimulated astrocytes, we examined their mitochondrial network dynamics.

Time-lapse experiments performed in astrocytes expressing *mito-GFP* revealed that, soon after LPS+IFNγ treatment, there was an overall reduction of the mitochondrial motility and an increase in the number of stationary organelles (**Figure 3E-3F**). To evaluate whether the observed changes were mirrored by corresponding alterations in the fusion-fission dynamics of mitochondria, astrocytes were co-transfected with *mito-DsRed* together with a photo-activatable *mito-GFP* (*mito-PAGFP*) (Karbowski et al., 2004) and photo-labelled mitochondria were followed by time-lapse microscopy at 4 and 24h after LPS+IFNγ stimulation (**Figure 3G**). While in control astrocytes the GFP signal displayed a progressive and constant diffusion from the photo-activated region of interest (inner ROI), indicative of ongoing mitochondrial fusion, in 4h-stimulated astrocytes these dynamics were virtually abolished (**Figure 3H-3J**). Consistent with a rescue of their morphology, by 24h mitochondria also re-acquired fusion dynamics similar to controls (**Figure 3I-3J**). Together, these results demonstrate that pro-inflammatory mediators severely alter mitochondrial network dynamics in astrocytes.

Recruitment of Drp1 onto mitochondria mediates their fragmentation during inflammation

We next assessed whether this mitochondrial phenotype in stimulated astrocytes was due to reduced fusion or, rather, to increased mitochondrial fission by evaluating the expression pattern of the major GTP-binding proteins known to govern mitochondrial dynamics (Liesa et al., 2009). Interestingly, immunoblot analysis of astrocytes treated with LPS+IFNγ revealed a substantial up-regulation of the pro-fission protein Drp1 by 4h after treatment **(Figure 4A)**. In contrast, no obvious changes in the expression pattern of the fusion proteins Mfn2 and Opa1 were observed **(Figure 4A)**. Also, direct evaluation of mitochondrial markers specific for the outer (TOM20) and inner

membranes (TIM44) and matrix (Hsp60) disclosed no overt alterations in the mitochondrial mass **(Figure 4A)**.

To gain further insights into the potential role of Drp1 we analyzed its phosphorylation state at Ser616 (hereafter referred to as P-Drp1), as phosphorylation at this site is known to promote the stabilization at the outer mitochondrial membrane of cytoplasmic Drp1, a key step required for mitochondrial fission (Chang and Blackstone, 2010). Indeed we observed a transient increase of P-Drp1 at 4h while, different from total Drp1 protein, P-Drp1 returned to control levels by 24h **(Figure 4A)**. Furthermore, by performing P-Drp1 immunocytochemistry we could observe a progressive increase of P-Drp1 immunoreactivity specifically localizing at mitochondria starting from 30 minutes-1h after LPS+IFNγ treatment, i.e. immediately before the onset of mitochondrial fragmentation, while it decreased to levels comparable to controls by 24h **(Figure 4B-4C)**. Conversely, total Drp1 remained relatively high up to 24h, the time when the tubular mitochondrial network was restored **(Figure 4C and Figure S6A)**. Of note, localization of endogenous Drp1 onto mitochondria appeared also increased in astrocytes of the lesion core *in vivo*, at the time (4dpi) when fragmentation was mostly evident **(Figure S6B)**.

This distinctive up-regulation and subsequent recruitment onto mitochondria strongly suggest Drp1 playing a central role in mitochondrial fragmentation during the inflammatory response. To validate this hypothesis, we specifically knocked-down Drp1 via RNA interference (**Figure S6C-S6D**). Astrocytes were transfected with scramble (miR-scr) or Drp1-targeting miRNAs (miR-Drp1) and the morphology of mitochondria evaluated at 4 and 24h after LPS+IFNγ treatment **(Figure 4D)**. Single-cell analysis showed that Drp1 knock-down prevented mitochondrial fragmentation at 4h (number of astrocytes showing fragmented mitochondria: 6.7% in miR-Drp1 versus 68.4% in miR-scramble; **Figure 4D-4E)** and, as expected, resulted in a

moderate increase in elongated mitochondria**.** A similar effect was obtained when a dominant negative mutant of Drp1 (K38E) (Neuspiel et al., 2005) was ectopically expressed in astrocytes prior stimulation **(Figure S6E-S6F)**. These results indicate that Drp1 activation is one of the key signalling events leading to fragmentation of mitochondria in astrocytes exposed to inflammatory stimuli.

Inhibition of iNOS prevents inflammation-mediated mitochondrial fragmentation in astrocytes

A main hallmark of inflammation in glia cells, including astrocytes, is the up-regulation of the inducible nitric oxide synthase (iNOS), which leads to nitric oxide (NO) production (Almeida et al., 2004; Brown et al., 1995). Several lines of evidence argue for a role of NO in regulating Drp1 activity and thus mitochondrial fission (Barsoum et al., 2006; Bossy et al., 2010; Cho et al., 2009). Therefore, we evaluated whether inflammation-induced NO production was required for mitochondrial fragmentation in astrocytes. As expected, we observed a time-dependent up-regulation of iNOS in cultured astrocytes exposed to LPS+IFNγ **(Figure 4F)**. Interestingly, pharmacological inhibition of iNOS with L-NAME or 1400W was able to prevent Drp1 activation and its recruitment onto mitochondria, ultimately impairing their fragmentation **(Figure 4G-4I)**. To validate the requirement of iNOS activity for mitochondrial remodelling in a more physiological context, we performed similar experiments in acute brain slices obtained from mito-RABV injected hGFAP-TVA mice **(Figure S7A)**. We first assessed by time-lapse imaging the responsiveness of astrocytic mitochondria to focally applied LPS+IFNγ, which consistently elicited a local increase in mitochondrial fission over time as shown above for IL-1β **(Figure S7B-S7C)**. By contrast, bath treatment of the iNOS inhibitor L-NAME starting from 30 minutes before LPS+IFNγ application was sufficient to prevent mitochondrial

fragmentation in astrocytes **(Figure S7D-S7E)**. Taken together, these data identify iNOS-mediated NO production and subsequent Drp1 activation as the key effectors transducing inflammatory insults into mitochondrial fission in astrocytes.

High ROS production and impaired mitochondrial respiration in stimulated astrocytes

The alterations in mitochondrial dynamics observed so far strongly suggest that these could contribute to the changes in the metabolic profile previously reported in astrocytes exposed to pro-inflammatory mediators (Almeida et al., 2004; Belanger et al., 2011b). To verify this hypothesis, we initially performed ATP measurements in stimulated astrocytes. In agreement with previous studies (Stewart et al., 1998) we observed a rapid and substantial increase in ATP production, which was virtually abolished when astrocytes were maintained in low glucose medium (**Figure S5D**), indicating that glycolysis becomes the predominant metabolic pathway producing ATP following stimulation with pro-inflammatory mediators. To gain further insights into the metabolic changes associated with mitochondria fragmentation, we measured their bioenergetics' capacity (oxygen consumption rate - OCR) in astrocytes exposed to LPS+IFNγ (Brand and Nicholls, 2011; Ferrick et al., 2008) **(Figure S5E)**. By 8h after treatment, i.e. at the peak of mitochondrial fragmentation, astrocytes displayed a significant reduction in the maximal respiration rate and spare respiratory capacity compared to controls (57.8 ± 0.6 and 53.6 ± 1.2%, respectively), indicating that mitochondrial functionality became impaired **(Figure 5A-5C)**. In contrast, by 24h about 80% of the maximal and spared respiratory capacity was recovered, suggesting an overall rescue of mitochondrial respiration at this time after stimulation **(Figure 5A-5C).**

This last observation prompted us to examine the extent of ROS generated in stimulated astrocytes, as these may increase following changes in mitochondrial

respiratory capacity, leading to oxidative damage and changes in redox signalling (Murphy, 2009). Astrocytes were treated with LPS+IFNγ and the production of mitochondrial ROS evaluated in intact cells using MitoSOX, a live-cell permeant indicator of mitochondrial superoxide (Gusdon et al., 2009). By 4h after treatment, ROS production in mitochondria was dramatically enhanced compared to control astrocytes (**Figure 5D**) and confocal microscopy analysis revealed high levels of ROS specifically co-localizing with fragmented mitochondria (**Figure 5E-5F**). Interestingly, ROS production decreased by 24h, in parallel with the re-establishment of tubular mitochondrial networks (**Figure 5E-5F**). Thus, pro-inflammatory stimuli lead to a transient production of ROS from mitochondria undergoing fragmentation.

Dysfunctional mitochondria are closely associated with autophagosomes

Given the transient nature of the mitochondrial dysfunction observed in response to inflammatory stimuli, we focused on the possible mechanisms regulating its resolution. One interesting possibility was the clearance of damaged mitochondria via autophagy, a form of quality control suggested to be important for maintaining the functionality of mitochondrial networks (Twig et al., 2008; Wang and Klionsky, 2011; Youle and Narendra, 2011). We thus examined whether autophagy was induced following LPS+IFNγ stimulation by evaluating the lipidation of the autophagy-related protein LC3 (its conversion from cytosolic to the autophagosomal-associated isoform LC3B-II) both under steady-state level and by using Bafilomycin A1, an inhibitor of lysosomal degradation widely used to examine LC3B-II turnover (Klionsky et al., 2012; Mizushima et al., 2010). We observed a significant increase in both the formation and maturation of new autophagosomes, starting by 2-4h and peaking around 8h post-treatment (**Figure 6A and S8A**). Likewise, the use of a DsRed-LC3-GFP reporter (Sheen et al., 2011) confirmed an increased autophagic flux following

this treatment (**Figure S8G-S8H**). Interestingly, a similar response could be elicited using other pro-inflammatory cytokines including IL-1β, IL-6 and TNF-α (**Figure S8B**). Finally, time-lapse video-microscopy of astrocytes co-transfected with *mito-DsRed* and *GFP-LC3* (Mizushima et al., 2010) revealed an increased formation of GFP+ autophagosomes following LPS+IFNγ treatment in live cells (**Figure S8C-S8F**). The temporal pattern of LC3B lipidation observed here precisely overlapped with the above-described alterations of the mitochondrial network, as many of the GFP+ autophagosomes co-localized with the DsRed signal originating from fragmented mitochondria in treated cells (**Figure S8F**). To further validate these results, we measured by immunostaining the conversion of endogenous LC3B to LC3B-II using a specific antibody recognizing LC3B-II. LPS+IFNγ treated astrocytes showed an overall increase in endogenous LC3B-II and a striking time-dependent co-localization with fragmented mitochondria (**Figure 6B-6C**). Importantly, the up-regulation of LC3B-II and its co-localization with mitochondria was detected in astrocytes expressing mito-GFP *in vivo* following cortical SW (**Figure 6D-6E**).

Electron microscopy, performed at 8h after LPS+IFNγ treatment, confirmed the presence of numerous autophagic vacuoles as compared to vehicle-treated astrocytes (**Figure 6F-6G**). Many of these autophagosomes were found in direct proximity or contact with fragmented mitochondria at 8h after stimulation (**Figure 6H**). In some cases, fragmented mitochondria were observed within double-membrane compartments (**Figure 6I**), possibly indicating the contribution of endoplasmic reticulum to the formation of new autophagosomes (Hamasaki et al., 2013). Interestingly, these double-membrane structures were absent at 24h, suggesting that only selected mitochondria had been targeted by autophagosomes for subsequent degradation.

To determine if this was the case, astrocytes expressing *mito-GFP* were treated with LPS+IFNγ for 4h or 24h and their mitochondria examined for co-localization with endogenous endosomal/lysosomal markers. At both analyzed time points, a significant proportion of fragmented mitochondria co-localized with the late-endosomal marker Rab7 (4h LPS+IFNγ: 30.0 ± 3.4%; 24h LPS+IFNγ: 19.5 ± 2.6%) compared to controls (5.1 ± 1.2%) (**Figure S9A-S9B**). In contrast, analysis of the lysosomal marker Lamp2 disclosed no significant co-localization at 4h after LPS+IFNγ treatment (8.9 ± 2.2%) compared to controls (6.3 ± 2.0%), but only at 24h (17.8 ± 2.9%) (**Figure S9B-S9C)**. Together, our data suggest that a proportion of dysfunctional mitochondria in stimulated astrocytes are targeted by autophagy for subsequent lysosomal degradation.

Blockade of autophagy impairs the restoration of tubular mitochondrial networks

To examine whether autophagy induction in response to pro-inflammatory stimuli could be an important mechanism to preserve mitochondrial integrity and avoid accumulation of potentially toxic metabolites (Wang and Klionsky, 2011; Youle and Narendra, 2011), we interfered with the autophagic cascade at two different levels. First, we deleted the gene encoding for *Atg7*, which is a key component of the autophagic machinery required for LC3B lipidation, by using astrocytes from $Atg7^{lox/lox}$ mice (Komatsu et al., 2005) and virus-mediated Cre expression. Virus transduction resulted in Atg7 protein loss by 5-7 days following Cre-mediated recombination (**Figure S10A**). As expected, Atg7 deletion substantially impaired the formation of new autophagosomes after LPS+IFNγ treatment (**Figure S10B-S10F**). At the single cell level and within this temporal window (5-7 days after recombination), deletion of *Atg7* did not significantly perturb the morphology of mitochondria in vehicle treated astrocytes (**Figure 7A-7B**). However, upon LPS+IFNγ treatment we observed that,

precisely at the time when control cells re-established a tubular mitochondrial network (24h), Atg7 knockout astrocytes showed widespread accumulations of clustered mitochondria, often resulting in the production of highly hyperfused networks (**Figure 7A-7B**). Likewise, over-expression of a dominant negative form of Atg4B, a protease required for proper processing of LC3 (Fujita et al., 2008), resulted in the formation of hyperfused mitochondrial clusters in stimulated astrocytes (**Figure S10I-S10J**). At the molecular level, we identified PKA/calcineurin-mediated phosphorylation of Drp1 at Ser637 to be increased in Atg7 knockout in comparison with control astrocytes (**Figure S10D**), suggesting that Drp1 retention in the cytoplasm contributes to the observed mitochondrial hyperfusion (Cribbs and Strack, 2007).

Interestingly, recent studies showed that mitochondria hyperfusion in mammalian cells subjected to starvation or cellular stress also promote cristae remodelling in order to transiently sustain energy production (Gomes et al., 2011; Tondera et al., 2009). Therefore, we examined here if this was also the case in our model. Conspicuously, EM analysis of mitochondria revealed a 24% increase ($p < 0.001$) in the density of cristae in Cre- versus GFP-transduced $Atg7^{lox/lox}$ astrocytes (**Figure 7C and S10G-S10H**) indicating that, in absence of autophagy, stimulated astrocytes undergo mitochondrial hyperfusion to increase cristae remodelling and possibly maintain ATP production (Gomes et al., 2011; Tondera et al., 2009). Nevertheless, *Atg7*-deficient astrocytes displayed prominent and prolonged generation of mitochondrial ROS as evaluated with MitoSOX, otherwise reduced in control astrocytes by 24h after treatment (**Figure 7D-7E**). Hence, while Atg7 knockout astrocytes can increase the number of cristae in response to a pro-inflammatory insult, their mitochondria keep generating non-physiological amounts of ROS, thus raising the question how long stimulated astrocytes can cope with the lack

of autophagy. Intriguingly, cell viability analyzed at 1 and 3 days after LPS+IFNγ stimulation revealed no evident changes between Atg7$^{lox/lox}$ astrocyte transduced with a Cre and Tomato or a Tomato-only (control) expressing virus (**Figure 7F**). However, by 8 days we detected a sharp increase in the number of Atg7-deficient astrocytes undergoing apoptosis (**Figure 7F-7G**), demonstrating that a failure in regenerating a tubular mitochondrial network ultimately affects astrocyte survival. Altogether, these results reveal autophagy to be a key mechanism for maintaining mitochondrial networks in astrocytes exposed to a pro-inflammatory environment (**Figure 7H**).

Discussion

Changes in mitochondrial dynamics are widely held to be associated with modifications in mitochondrial function (Gomes et al., 2011; Liesa et al., 2009). Given the growing evidence for a role of astroglia in both brain energy metabolism (Belanger et al., 2011a; Hertz et al., 2007) and disease (Sofroniew, 2009), in the present study we have addressed how mitochondrial dynamics may change in astrocytes directly exposed to pro-inflammatory mediators, a condition taking place *in vivo* following brain injury and the ensuing activation/recruitment of local (microglia) and circulating (leukocytes) pro-inflammatory cells (Hamby et al., 2012; Zamanian et al., 2012). Interestingly, in contrast to the prevailing assumption that astrogliosis identifies a common state shared by reactive astrocytes, our results reveal heterogeneity with respect to mitochondrial dynamics between the lesion core and penumbra. In particular, we show that inflammatory stimuli induce rapid and profound changes of the mitochondrial network leading to its fragmentation and impaired respiration rate. We also show that the resolution of this response, mediated by the pro-fission protein Drp1, is crucially dependent on a timely induction of autophagy,

revealing a state-dependent control of the mitochondrial network in astroglia. Thus, region-specific differences in the mitochondrial response of reactive astrocytes may reveal previously unknown forms of mitochondrial plasticity important for adjusting the astrocyte metabolic state and possibly ensuring adequate energy production during the metabolic challenge that follows brain injury and inflammation.

Although fragmentation of mitochondria in mammalian cells often precedes apoptosis (Youle and van der Bliek, 2012), we observed no obvious changes in astrocyte survival, consistent with the well known resistance of astrocytes to inflammatory stimuli (Bardehle et al., 2013; Brown et al., 1995; Stewart et al., 1998). Rather, we detected a prompt autophagic response as an essential mechanism of mitochondrial quality control and presumably important for maintaining a functional mitochondrial respiration. Surprisingly, wild-type astrocytes were never found significantly depleted of mitochondria at any time point analyzed, as it would be expected in case of mitophagy (Twig et al., 2008; Wang and Klionsky, 2011; Youle and van der Bliek, 2012). Nevertheless, our data demonstrate that newly-formed autophagosomes efficiently target a specific subpopulation of fragmented mitochondria causing their selective removal from the network. The significance of this response became clear when the same experiments were performed in *Atg7* knockout astrocytes, which failed to restore tubular networks. This led to the accumulation of highly hyperfused mitochondria, ROS and ultimately to cell death, demonstrating the crucial role of autophagy in clearing damaged mitochondria and rapidly regenerating a physiological network under high stress conditions (**Figure 7H**). On the other side, the mitochondrial hyperfusion observed in *Atg7*-deficient astrocytes is highly reminiscent of the mitochondrial elongation described in mammalian cells subjected to starvation or stress, a response shown to sustain ATP production (Gomes et al., 2011; Rambold et al., 2011; Tondera et al., 2009).

Interestingly, this mitochondrial hyperelongation can occur in absence of functional autophagic machinery, suggesting that mitochondrial dynamics can operate independently from autophagy. Supporting this parallelism, by 24h after stimulation *Atg7* knockout astrocytes displayed increased cristae formation. While this mitochondrial remodelling may therefore represent a mechanism for compensating failing energy production, the fact that astrocyte survival is impaired at longer times demonstrates that hyperfusion of mitochondria can only transiently sustain cell metabolism (Rolland et al., 2013), and that autophagy is important for re-establishing a physiological mitochondrial architecture following inflammation.

In summary, our results identify a direct link between inflammation and the changes in mitochondrial dynamics - and ultimately bioenergetics - of astroglial cells, revealing a mechanism through which astrocytes handle the metabolic challenge that follows brain injury. Intriguingly, the *in vivo* spatial organization of astrocytic mitochondria, often found in direct proximity of adjacent neuronal bodies and dendrites, argues for their participation in sustaining local demand of metabolites and ions at critical astrocyte-neuron points of contact. If this is the case, alterations in astrocyte mitochondrial bioenergetics may in turn affect neuronal functioning and/or survival, and thus appropriate mechanisms of mitochondrial quality-control in astrocytes could be of great significance for locally regulating metabolic coupling during neuroinflammation. Providing further insights on how inflammatory processes impact local bioenergetics within damaged brain tissue may pave new ways to understand the link between neuroinflammation and neuronal cell death.

Experimental procedures

Astrocyte cultures

Primary cultures of cortical astrocytes were prepared from postnatal day 1-2 wild-type and Atg7$^{loxP/loxP}$ mice (provided by M. Komatsu) as previously described (Bergami et al., 2008) and mantained in DMEM-F12 with 10% fetal bovine serum (GIBCO) at 37°C in 5% CO2. Flasks were shaked every 3 days and medium replaced until confluency was reached (about 2-3 weeks after plating).

Mice, stereotactic injections and stab wound

Six to 8-week old C57BL/6J, hGFAP-GFP and hGFAP-TVA transgenic mice were used for stereotactic injections, SW (Bardehle et al., 2013) and slice imaging. All experimental procedures were performed in agreement with the European Union and German guidelines and were approved by the Government of State of Upper Bavaria. *See online SI*.

Histology and immunostainings

Immunostainings were performed as previously described (Bergami et al., 2008). *See online SI.*

Imaging and quantitative analysis

Samples were imaged with a confocal laser-scanning microscope (LSM 710, Zeiss) equipped with 4 laser lines (405, 488, 561 and 633 nm) and 10x (NA 0.3), 25x (NA 0.8), 40x (NA 1.1) or 63x (NA 1.3) objectives. For imaging of mitochondrial morphology, serial z-stacks of 0.3µm or 0.5µm were acquired with a digital zoom of 2 or 3 (63x objective). ROIs corresponding to the shape of individual mitochondria were manually drawn through stacks and the distribution of their length plotted against

their frequency. Mitochondrial phenotype in astrocytes was based on the appearance of mitochondria (>70% of the total mitochondrial pool) using mitochondrial markers or mito-GFP. Mitochondria were classified depending on their length in fragmented, tubular or elongated/hyperfused. Quantification of cells expressing specific markers was performed off-line on confocal acquisitions. As capillary penetration through the *dura mater* could lead by itself to a slight activation of glial cells in layer I of the cortex **(Figure S3A)**, analysis of mitochondrial morphology *in vivo* was restricted to cortical layers II/III and deeper layers, thus reducing the possibility to underestimate any phenotype obtained in SW experiments. Location of astrocytes with respect to SW was assessed depending on their GFAP expression (high in the penumbra, low in the lesion core) and relative density of CD45+ cells. Assessment of mitochondrial morphology and membrane potential in mito-RABV transduced astrocytes revealed that low titre virus (Ortinski et al., 2010) did not visibly affect their physiology up to 10 days after transduction (**Figure S1F-S1H**). *See online SI*.

Statistical analysis

Results are presented as means ± SEM. Graphical illustrations and significance were obtained with GraphPad Prism 5 (GraphPad Software, San Diego, CA) using the Student's *t*-test or the multiple comparison ANOVA, followed by Bonferroni's as a post-hoc test, unless otherwise indicated.

References

Almeida, A., Almeida, J., Bolanos, J.P., and Moncada, S. (2001). Different responses of astrocytes and neurons to nitric oxide: the role of glycolytically generated ATP in astrocyte protection. Proc Natl Acad Sci U S A 98, 15294-15299.

Almeida, A., Moncada, S., and Bolanos, J.P. (2004). Nitric oxide switches on glycolysis through the AMP protein kinase and 6-phosphofructo-2-kinase pathway. Nat Cell Biol 6, 45-51.

Angeloni, C., Motori, E., Fabbri, D., Malaguti, M., Leoncini, E., Lorenzini, A., and Hrelia, S. (2011). H2O2 preconditioning modulates phase II enzymes through p38 MAPK and PI3K/Akt activation. American journal of physiology. Heart and circulatory physiology 300, H2196-2205.

Bardehle, S., Kruger, M., Buggenthin, F., Schwausch, J., Ninkovic, J., Clevers, H., Snippert, H.J., Theis, F.J., Meyer-Luehmann, M., Bechmann, I., et al. (2013). Live imaging of astrocyte responses to acute injury reveals selective juxtavascular proliferation. Nat Neurosci 16, 580-586.

Barsoum, M.J., Yuan, H., Gerencser, A.A., Liot, G., Kushnareva, Y., Graber, S., Kovacs, I., Lee, W.D., Waggoner, J., Cui, J., et al. (2006). Nitric oxide-induced mitochondrial fission is regulated by dynamin-related GTPases in neurons. EMBO J 25, 3900-3911.

Belanger, M., Allaman, I., and Magistretti, P.J. (2011a). Brain energy metabolism: focus on astrocyte-neuron metabolic cooperation. Cell Metab 14, 724-738.

Belanger, M., Allaman, I., and Magistretti, P.J. (2011b). Differential effects of pro- and anti-inflammatory cytokines alone or in combinations on the metabolic profile of astrocytes. J Neurochem 116, 564-576.

Bergami, M., Santi, S., Formaggio, E., Cagnoli, C., Verderio, C., Blum, R., Berninger, B., Matteoli, M., and Canossa, M. (2008). Uptake and recycling of pro-BDNF for transmitter-induced secretion by cortical astrocytes. J Cell Biol 183, 213-221.

Bethea, J.R., Nagashima, H., Acosta, M.C., Briceno, C., Gomez, F., Marcillo, A.E., Loor, K., Green, J., and Dietrich, W.D. (1999). Systemically administered interleukin-10 reduces tumor necrosis factor-alpha production and significantly improves functional recovery following traumatic spinal cord injury in rats. Journal of neurotrauma 16, 851-863.

Bossy, B., Petrilli, A., Klinglmayr, E., Chen, J., Lutz-Meindl, U., Knott, A.B., Masliah, E., Schwarzenbacher, R., and Bossy-Wetzel, E. (2010). S-Nitrosylation of DRP1 does not affect enzymatic activity and is not specific to Alzheimer's disease. J Alzheimers Dis 20 Suppl 2, S513-526.

Brand, M.D., and Nicholls, D.G. (2011). Assessing mitochondrial dysfunction in cells. Biochem J 435, 297-312.

Brown, G.C., Bolanos, J.P., Heales, S.J., and Clark, J.B. (1995). Nitric oxide produced by activated astrocytes rapidly and reversibly inhibits cellular respiration. Neurosci Lett 193, 201-204.

Bush, T.G., Puvanachandra, N., Horner, C.H., Polito, A., Ostenfeld, T., Svendsen, C.N., Mucke, L., Johnson, M.H., and Sofroniew, M.V. (1999). Leukocyte infiltration, neuronal degeneration, and neurite outgrowth after ablation of scar-forming, reactive astrocytes in adult transgenic mice. Neuron 23, 297-308.

Chang, C.R., and Blackstone, C. (2010). Dynamic regulation of mitochondrial fission through modification of the dynamin-related protein Drp1. Ann N Y Acad Sci 1201, 34-39.

Cho, D.H., Nakamura, T., Fang, J., Cieplak, P., Godzik, A., Gu, Z., and Lipton, S.A. (2009). S-nitrosylation of Drp1 mediates beta-amyloid-related mitochondrial fission and neuronal injury. Science 324, 102-105.

Cribbs, J.T., and Strack, S. (2007). Reversible phosphorylation of Drp1 by cyclic AMP-dependent protein kinase and calcineurin regulates mitochondrial fission and cell death. EMBO Rep 8, 939-944.

Detmer, S.A., and Chan, D.C. (2007). Functions and dysfunctions of mitochondrial dynamics. Nat Rev Mol Cell Biol 8, 870-879.

Farina, C., Aloisi, F., and Meinl, E. (2007). Astrocytes are active players in cerebral innate immunity. Trends Immunol 28, 138-145.

Ferrick, D.A., Neilson, A., and Beeson, C. (2008). Advances in measuring cellular bioenergetics using extracellular flux. Drug Discov Today 13, 268-274.

Finke, S., Mueller-Waldeck, R., and Conzelmann, K.K. (2003). Rabies virus matrix protein regulates the balance of virus transcription and replication. The Journal of general virology 84, 1613-1621.

Fujita, N., Hayashi-Nishino, M., Fukumoto, H., Omori, H., Yamamoto, A., Noda, T., and Yoshimori, T. (2008). An Atg4B mutant hampers the lipidation of LC3 paralogues and causes defects in autophagosome closure. Mol Biol Cell 19, 4651-4659.

Ghanem, A., Kern, A., and Conzelmann, K.K. (2012). Significantly improved rescue of rabies virus from cDNA plasmids. European journal of cell biology 91, 10-16.

Gomes, L.C., Di Benedetto, G., and Scorrano, L. (2011). During autophagy mitochondria elongate, are spared from degradation and sustain cell viability. Nat Cell Biol 13, 589-598.

Gusdon, A.M., Chen, J., Votyakova, T.V., and Mathews, C.E. (2009). Chapter 24 Quantification, localization, and tissue specificities of mouse mitochondrial reactive oxygen species production. Methods Enzymol 456, 439-457.

Halassa, M.M., Fellin, T., and Haydon, P.G. (2007). The tripartite synapse: roles for gliotransmission in health and disease. Trends Mol Med 13, 54-63.

Hamasaki, M., Furuta, N., Matsuda, A., Nezu, A., Yamamoto, A., Fujita, N., Oomori, H., Noda, T., Haraguchi, T., Hiraoka, Y., et al. (2013). Autophagosomes form at ER-mitochondria contact sites. Nature 495, 389-393.

Hamby, M.E., Coppola, G., Ao, Y., Geschwind, D.H., Khakh, B.S., and Sofroniew, M.V. (2012). Inflammatory mediators alter the astrocyte transcriptome and calcium signaling elicited by multiple g-protein-coupled receptors. J Neurosci 32, 14489-14510.

Hertz, L., Peng, L., and Dienel, G.A. (2007). Energy metabolism in astrocytes: high rate of oxidative metabolism and spatiotemporal dependence on glycolysis/glycogenolysis. J Cereb Blood Flow Metab 27, 219-249.

Holland, E.C., and Varmus, H.E. (1998). Basic fibroblast growth factor induces cell migration and proliferation after glia-specific gene transfer in mice. Proc Natl Acad Sci U S A 95, 1218-1223.

Iadecola, C., and Nedergaard, M. (2007). Glial regulation of the cerebral microvasculature. Nat Neurosci 10, 1369-1376.

Kamm, K., Vanderkolk, W., Lawrence, C., Jonker, M., and Davis, A.T. (2006). The effect of traumatic brain injury upon the concentration and expression of interleukin-1beta and interleukin-10 in the rat. The Journal of trauma 60, 152-157.

Karbowski, M., Arnoult, D., Chen, H., Chan, D.C., Smith, C.L., and Youle, R.J. (2004). Quantitation of mitochondrial dynamics by photolabeling of individual organelles shows that mitochondrial fusion is blocked during the Bax activation phase of apoptosis. J Cell Biol 164, 493-499.

Kasischke, K.A., Vishwasrao, H.D., Fisher, P.J., Zipfel, W.R., and Webb, W.W. (2004). Neural activity triggers neuronal oxidative metabolism followed by astrocytic glycolysis. Science 305, 99-103.

Klionsky, D.J., Abdalla, F.C., Abeliovich, H., Abraham, R.T., Acevedo-Arozena, A., Adeli, K., Agholme, L., Agnello, M., Agostinis, P., Aguirre-Ghiso, J.A., et al. (2012). Guidelines for the use and interpretation of assays for monitoring autophagy. Autophagy 8, 445-544.

Knott, A.B., Perkins, G., Schwarzenbacher, R., and Bossy-Wetzel, E. (2008). Mitochondrial fragmentation in neurodegeneration. Nat Rev Neurosci 9, 505-518.

Komatsu, M., Waguri, S., Ueno, T., Iwata, J., Murata, S., Tanida, I., Ezaki, J., Mizushima, N., Ohsumi, Y., Uchiyama, Y., et al. (2005). Impairment of starvation-induced and constitutive autophagy in Atg7-deficient mice. J Cell Biol 169, 425-434.

Liesa, M., Palacin, M., and Zorzano, A. (2009). Mitochondrial dynamics in mammalian health and disease. Physiol Rev 89, 799-845.

Lovatt, D., Sonnewald, U., Waagepetersen, H.S., Schousboe, A., He, W., Lin, J.H., Han, X., Takano, T., Wang, S., Sim, F.J., et al. (2007). The transcriptome and metabolic gene signature of protoplasmic astrocytes in the adult murine cortex. J Neurosci 27, 12255-12266.

Mathiisen, T.M., Lehre, K.P., Danbolt, N.C., and Ottersen, O.P. (2010). The perivascular astroglial sheath provides a complete covering of the brain microvessels: an electron microscopic 3D reconstruction. Glia 58, 1094-1103.

Menet, V., Prieto, M., Privat, A., and Gimenez y Ribotta, M. (2003). Axonal plasticity and functional recovery after spinal cord injury in mice deficient in both glial fibrillary acidic protein and vimentin genes. Proc Natl Acad Sci U S A 100, 8999-9004.

Mizushima, N., Yoshimori, T., and Levine, B. (2010). Methods in mammalian autophagy research. Cell 140, 313-326.

Murphy, M.P. (2009). How mitochondria produce reactive oxygen species. Biochem J 417, 1-13.

Neuspiel, M., Zunino, R., Gangaraju, S., Rippstein, P., and McBride, H. (2005). Activated mitofusin 2 signals mitochondrial fusion, interferes with Bax activation, and reduces susceptibility to radical induced depolarization. J Biol Chem 280, 25060-25070.

Okada, S., Nakamura, M., Katoh, H., Miyao, T., Shimazaki, T., Ishii, K., Yamane, J., Yoshimura, A., Iwamoto, Y., Toyama, Y., et al. (2006). Conditional ablation of Stat3 or Socs3 discloses a dual role for reactive astrocytes after spinal cord injury. Nat Med 12, 829-834.

Ortinski, P.I., Dong, J., Mungenast, A., Yue, C., Takano, H., Watson, D.J., Haydon, P.G., and Coulter, D.A. (2010). Selective induction of astrocytic gliosis generates deficits in neuronal inhibition. Nat Neurosci 13, 584-591.

Pinteaux, E., Trotter, P., and Simi, A. (2009). Cell-specific and concentration-dependent actions of interleukin-1 in acute brain inflammation. Cytokine 45, 1-7.

Rambold, A.S., Kostelecky, B., Elia, N., and Lippincott-Schwartz, J. (2011). Tubular network formation protects mitochondria from autophagosomal degradation during nutrient starvation. Proc Natl Acad Sci U S A 108, 10190-10195.

Rolland, S.G., Motori, E., Memar, N., Hench, J., Frank, S., Winklhofer, K.F., and Conradt, B. (2013). Impaired complex IV activity in response to loss of LRPPRC function can be compensated by mitochondrial hyperfusion. Proc Natl Acad Sci U S A 110, E2967-2976.

Sheen, J.H., Zoncu, R., Kim, D., and Sabatini, D.M. (2011). Defective regulation of autophagy upon leucine deprivation reveals a targetable liability of human melanoma cells in vitro and in vivo. Cancer cell 19, 613-628.

Sofroniew, M.V. (2009). Molecular dissection of reactive astrogliosis and glial scar formation. Trends Neurosci 32, 638-647.

Stewart, V.C., Taylor, B., Bolanos, J.P., Land, J.M., Clark, J.B., and Heales, S.J. (1998). Astrocytic mitochondrial respiratory chain damage: effect on cellular ATP levels. Biochem Soc Trans 26, S346.

Tondera, D., Grandemange, S., Jourdain, A., Karbowski, M., Mattenberger, Y., Herzig, S., Da Cruz, S., Clerc, P., Raschke, I., Merkwirth, C., et al. (2009). SLP-2 is required for stress-induced mitochondrial hyperfusion. EMBO J 28, 1589-1600.

Twig, G., Elorza, A., Molina, A.J., Mohamed, H., Wikstrom, J.D., Walzer, G., Stiles, L., Haigh, S.E., Katz, S., Las, G., et al. (2008). Fission and selective fusion govern mitochondrial segregation and elimination by autophagy. EMBO J 27, 433-446.

Wang, K., and Klionsky, D.J. (2011). Mitochondria removal by autophagy. Autophagy 7, 297-300.

Wickersham, I.R., Finke, S., Conzelmann, K.K., and Callaway, E.M. (2007a). Retrograde neuronal tracing with a deletion-mutant rabies virus. Nat Methods 4, 47-49.

Wickersham, I.R., Lyon, D.C., Barnard, R.J., Mori, T., Finke, S., Conzelmann, K.K., Young, J.A., and Callaway, E.M. (2007b). Monosynaptic restriction of transsynaptic tracing from single, genetically targeted neurons. Neuron 53, 639-647.

Wilhelmsson, U., Bushong, E.A., Price, D.L., Smarr, B.L., Phung, V., Terada, M., Ellisman, M.H., and Pekny, M. (2006). Redefining the concept of reactive astrocytes as cells that remain within their unique domains upon reaction to injury. Proc Natl Acad Sci U S A 103, 17513-17518.

Youle, R.J., and Narendra, D.P. (2011). Mechanisms of mitophagy. Nat Rev Mol Cell Biol 12, 9-14.

Youle, R.J., and van der Bliek, A.M. (2012). Mitochondrial fission, fusion, and stress. Science 337, 1062-1065.

Zamanian, J.L., Xu, L., Foo, L.C., Nouri, N., Zhou, L., Giffard, R.G., and Barres, B.A. (2012). Genomic analysis of reactive astrogliosis. J Neurosci 32, 6391-6410.

Author contributions

E.M. and M.B. conceived and designed experiments, carried out imaging of mitochondria in slice, analyzed the data, prepared figures and wrote the manuscript. E.M. performed all the *in vitro* experiments. M.B. performed virus injections. N.T. and J.P. performed EM studies and analyses. A.G. and K.K.C. provided RABV. C.A. and M.M. analyzed cytofluorimetric assays. B.B., M.G. and K.F.W. provided conceptual advice. G.C.F., B.B., M.G., K.F.W., S.H. and M.B. provided financial support. All authors discussed the data and critically revised the manuscript. S.H. and M.B. supervised the project.

Acknowledgements

We thank T. Fellin, P. Grafe and T. Misgeld for insightful comments and suggestions; M. Stanke for hGFAP-TVA mice; D. Paquet and F. Rucker for excellent assistance with time-lapse microscopy; G. Masserdotti and A. Lepier for assistance with virus preparation; the Electron Microscopy Facility at the University of Lausanne for the use of electron microscopes and J. Kocher-Braissant for help with tissue processing. M. Komatsu for providing Atg7 floxed mice. T. Misgeld and M. Brill for help with Atg7 mice. C. Schweimer, P. Apostolopoulos, N. Zapf, I. Muehlhahn, D. Franzen and G. Jaege for technical assistance. This work was supported by the Swiss National Science foundation to J.P. and N.T., by the “Fondation Leenaards” to N.T., by the SFB870 (Deutsche Forschungsgemeinschaft) to K.K.C and M.G., by the Deutsche Forschungsgemeinschaft, the BMBF (NGFN plus "Functional Genomics of Parkinson's Disease), and the Helmholtz Alliance (Mental Health in an Ageing Society) to K.F.W., by MIUR-FIRB (project RBAP11HSZS) and “Fondazione del Monte di Bologna e Ravenna” to E.M., M.M., C.A., G.C.F. and S.H.; by the Bavarian State Ministry of Sciences, Research and the Arts (ForNeuroCell) to B.B. and M.G.

795 and by the LMU Research Fellowship program to M.B.. The authors declare no
796 competing financial interests.

797

798

Figure legends

Figure 1. Region-specific remodelling of astrocyte mitochondrial networks following SW. (A) Experimental plan for targeting *mito-GFP* via mito-RABV infusion selectively to astrocytes in hGFAP-*TVA* mice. **(B)** Example of mito-RABV delivery at 4 days post injection (dpi) of mito-RABV. Transduced cells (lower panels) express the astrocytic marker S100β. Bars 100 and 20 µm. **(C)** Histogram reporting on the efficiency of mito-RABV in targeting astrocytes in hGFAP-TVA mice (n=3 mice, 200-300 cells/mouse; ***, $p < 0.001$). **(D)** Experimental plan for combining mito-RABV infusion with stab wound (SW) injury, followed by morphometric analysis. **(E)** Example of cortical SW at 4dpi in mito-RABV injected mice. Enlargements depict the "core" and "penumbra" (or forming scar) regions, defined according to GFAP and S100β immunostainings. Bars 200µm. **(F)** Astrocyte mitochondrial morphologies observed following SW. Yellow arrowheads point to altered mitochondrial morphology (elongated or fragmented) compared to control astrocytes of non-lesioned cortices. Nuclear staining and immunoreactivity for GFAP and S100β (white arrowheads) for each example are shown. Bars 15µm. **(G)** Distribution of the mitochondrial length in astrocytes located within the lesion core. Inset reports on the average mitochondrial length (n=6 cells/time point, 70-150 mitochondria/cell). **(H)** Quantification of the mitochondrial phenotype at each indicated time point after SW (n=3 mice/time point, 100-200 cells/mouse). ***, $p<0.001$. *See also Figures S1 and S3*.

Figure 2. Pro-inflammatory cytokines elicit local changes in astrocyte mitochondrial dynamics. (A) Accumulation of CD45+ pro-inflammatory cells within the lesion core at 4dpi following SW. Bars 80µm. **(B)** Region-specific density of CD45+ cells at 4dpi following SW (n=3 mice). **(C)** Immunoreactivity for IL-1β following

SW. Enlargements show IL-1β+ cells (arrowheads) surrounding a mito-GFP expressing astrocyte in the lesion core. Bars 100 and 20 µm. **(D)** Experimental plan for imaging astrocyte mitochondrial dynamics in brain slices. Branches were grouped into proximal (quadrant I) or distal (quadrants II-IV) from the releasing pipette. **(E)** Confocal picture showing the local application of Alexa488 to a single transduced astrocyte in slice. Bar 20µm. **(F)** Time-lapse of individual mitochondria showing fusion and fission events (arrowhead: stable mitochondrion). Bar 5µm. **(G)** Example of mitochondrial dynamics occurring within the proximal branches (boxed in red) during focal application of IL-1β. Lower panels show selected time-lapse frames of the boxed area illustrating the prevalence of fission events (see percentages). Bars 5µm. **(H)** Example showing distal branches (boxed in grey) during application of IL-1β. Lower panels show the prevalence of fusion events. Bars 5µm. **(I)** Index of fission-fusion for each quadrant and for whole astrocytes during IL-1β application (n=5 cells; *, $p< 0.05$; **, $p< 0.01$). **(J)** Percentages of fusion and fission events for each quadrant during IL-1β focal application. **(K)** Index of fission-fusion during ACSF-only application (n=5 cells). **(L)** Percentages of fusion and fission events for each quadrant during ACSF focal application. *See also Figures S3 and S4*.

Figure 3. Pro-inflammatory stimuli induce rapid but transient alterations of mitochondrial dynamics in cultured cortical astrocytes. (A) Astrocyte (GFAP+) cultures used in this study. Bar 30µm. **(B)** Morphology of mitochondria in individual astrocytes at different times after LPS+IFNγ treatment. Bars 10µm. **(C)** Changes in mitochondrial length after LPS+IFNγ treatment (n=15 cells/condition, 20-30 mitochondria per cell). **(D)** Average mitochondrial length (n=15 cells/condition, 20-30 mitochondria per cell; ***, $p< 0.001$). **(E)** Time-lapse imaging of mitochondria in a

mito-GFP expressing astrocyte and relative classification according to their motility (stationary: 0-0.2 µm; moving: 0.3-1 µm; fast moving: >1 µm). Colour-coded tracks of representative examples are shown. Bar 5 µm. **(F)** Quantification of mitochondrial motility in astrocytes after LPS+IFNγ treatment compared to controls (n=3 cells; 15 mitochondria per cell; *, p< 0.05). **(G)** Experimental plan used for assessing mitochondrial fusion proficiency in control or LPS+IFNγ treated astrocytes. The rate of diffusion of mito-PAGFP signal after ROI photoactivation was used to estimate the extent of mitochondrial fusion. **(H)** Example of photoactivated control (top) and LPS+IFNγ treated astrocytes (4h, bottom) co-expressing mito-DsRed and mito-PAGFP. Right panels show time-lapse frames of the photoactivated area in both examples. Bars 10µm. **(I)** Quantification of GFP signal within the initial ROI of photoactivation over 45' of imaging (n=6 cells). **(J)** Quantification of GFP signal in the outer ROI as depicted in **G** (n=6 cells). *See also Figure S5*.

Figure 4. Drp1-mediated and iNOS-dependent mitochondrial fragmentation in stimulated astrocytes. (A) Expression levels of mitochondrial proteins regulating fission (Drp1 and its phosphorylated form at serine 616, P-Drp1) or fusion (Opa1 and Mfn2) and that of markers indicative of mitochondrial mass (Tom20, Tim44, Hsp60) in control astrocytes or following LPS+IFNγ treatment. **(B)** Immunostaining for P-Drp1 and the mitochondrial marker Hsp60 at different time-points following treatment. Surface rendering of the areas boxed in yellow highlights the time-dependent recruitment of P-Drp1 on mitochondria. Bars 5µm. **(C)** Quantification of P-Drp1+ punctae (grey line) per unit of mitochondrial length with respect to the mitochondrial only (black line) or entire cell (per area unit; red line) density of total Drp1+ punctae (n=3-5 cells/time point; 10-20 mitochondria/cell). **(D)** Confocal pictures showing the

morphology of mitochondria following transfection with GFP-encoding scramble (miR-scr) or Drp1 miRNA (miR-Drp1). Bars 5µm. **(E)** Quantification of the mitochondrial phenotype (tubular, fragmented or elongated) in astrocytes transfected with miR-scr or miR-Drp1 and treated with LPS+IFNγ (n=3 independent experiments, 50-100 cells/time point; ***, p< 0.001). **(F)** Expression of iNOS in astrocytes following LPS+IFNγ treatment. **(G)** P-Drp1 immunostaining in stimulated astrocytes in absence or presence of L-NAME. Bars 5µm. **(H)** Quantification of P-Drp1+ punctae for unit of mitochondrial length in stimulated astrocytes co-treated or not with L-NAME (n=3 cells/time point, 10-20 mitochondria/cell; *, p< 0.05; **, p< 0.01). **(I)** Quantification of the mitochondrial phenotype in stimulated astrocytes in absence or presence of the iNOS inhibitors L-NAME or 1400W (n=3 experiments, 30-70 cells/time point; ***, p< 0.001). *See also Figures S6 and S7.*

Figure 5. LPS+IFNγ treatment transiently impairs mitochondrial respiration and leads to ROS production. (A) Respirometric analysis (oxygen consumption rate; OCR) of control and LPS+IFNγ stimulated astrocytes (8 and 24h). **(B)** Histogram showing the averaged values of maximal respiratory capacity and **(C)** spare respiratory capacity in controls, 8 and 24h-stimulated astrocytes (n=3-5 independent experiments; *, p< 0.05; Kruskal-Wallis test). **(D)** Confocal pictures depicting the fluorescence intensity of MitoSOX Red in control and LPS+IFNγ treated astrocytes. After MitoSOX live-imaging, samples were fixed and subjected to immunostaining for normalization on Tom20. Enlargements of the boxed areas show single and merged channels of MitoSOX and Tom20. Arrowheads point to individual mitochondria in stimulated astrocytes. N: nucleus. Bars 10µm. **(E)** Linescan analysis of the examples (circles) shown in **D** reporting on the intensity levels of MitoSOX in individual

mitochondria. **(F)** Fluorescence intensity of MitoSOX analyzed as shown in **E** and normalized to Tom20 immunoreactivity (n=6 cells/condition, 10-15 mitochondria/cell; ***, p< 0.001). *See also Figures S5.*

Figure 6. Pro-inflammatory stimuli increase autophagosome formation and their association with mitochondria in astrocytes. (A) Temporal pattern of LC3B conversion after astrocyte stimulation with LPS+IFNγ. Immunoblots show experiments conducted in absence or presence of bafilomycin A1 (100nM, 12h) to assess the autophagic flux. **(B)** Immunostaining showing endogenous LC3B-II expression and its co-localization with fragmented mitochondria (arrowheads) following stimulation. Right panels illustrate surface rendering of the boxed areas. Bar 5µm. **(C)** Co-localization analysis of endogenous LC3B-II and Hsp60 at different times after astrocytes stimulation (n=10 cells/time point; **, p< 0.01; ***, p< 0.001). **(D)** Expression levels of LC3B-II and relative co-localization with mito-GFP *in vivo* at 4dpi. **(E)** Quantification of endogenous LC3B-II co-localization with mito-GFP *in vivo* at 4dpi (n=5 cells; **, p< 0.01). **(F)** Electron micrographs of control or LPS+IFNγ treated astrocytes. Several autophagic vacuoles (red arrowheads) were clearly visible in the treated condition. High magnifications of the boxed areas are shown. Bars 10µm. **(G)** Histogram showing the density per cell of autophagic vacuoles (n=5-15 cells/condition; ***, p< 0.001). **(H)** Example of treated astrocytes showing several mitochondria (red arrowheads) in proximity of an autophagic vacuole. Bar 1µm. **(I)** Example showing several double-membrane structures containing fragmented mitochondria (red arrowheads) and possibly indicating the contribution of endoplasmic reticulum to the formation of new autophagosomes. Enlargement of the boxed area is shown. Bars 1µm. *See also Figures S8 and S9.*

Figure 7. Autophagy is required for regenerating tubular mitochondrial networks following pro-inflammatory stimulation. (A) Examples of Atg7$^{lox/lox}$ astrocytes transduced with either a GFP-only or a Cre and GFP-encoding virus and analyzed for their mitochondrial morphology. Magnifications of the boxed areas and classification of mitochondrial morphologies are shown. Yellow arrowheads point to hyperfused/clustered mitochondria. Bars 10µm. **(B)** Quantification of the mitochondrial phenotype in Atg7$^{lox/lox}$ astrocytes in presence of absence of LPS+IFNγ stimulation (n=3 independent experiments, 50-100 cells/time point; **, p< 0.01). **(C)** EM pictures showing mitochondrial cristae in Atg7-deficient and control astrocytes. **(D)** Examples of Atg7$^{lox/lox}$ astrocytes examined for ROS production following LPS+IFNγ treatment. Panels report on MitoSOX fluorescence intensity of transduced cells (in pseudocolors) at low and high magnifications. Arrowheads point to transduced astrocytes at 24h after treatment. Bars 10µm. **(E)** Quantification of MitoSOX fluorescence intensity in control or stimulated Atg7$^{lox/lox}$ astrocytes (n=5 cells/condition, 10 mitochondria/cell; **, p< 0.01). **(F)** Survival assay of Atg7$^{lox/lox}$ astrocytes performed at 1, 3 and 8 days after stimulation with LPS+IFNγ (n=3 independent experiments, 300-600 cells/experiment and time point; ***, p< 0.001). **(G)** Confocal pictures showing Atg7$^{lox/lox}$ astrocytes transduced with control (Tomato-only) or Cre and Tomato-expressing viruses and immunostained for Caspase 3-active at 8 days following stimulation. Bar 50µm. **(H)** Summary of the mitochondrial alterations taking place in astrocyte following stimulation with pro-inflammatory mediators. *See also Figure S10.*

Supplemental information

Supplemental Methods

Stereotactic injections and stab wound

For surgery, mice were anesthetized and a portion of the skull covering the somatosensory cortex (from Bregma: caudal 2.0, lateral 1.8) was thinned with a dental drill. A bended syringe needle was used to carefully create a small perforation of the skull, avoiding disturbing the underlying vasculature. A finely pulled glass capillary was then slowly inserted through the micro-perforation (from Bregma: ventral -0.5 to -0.3) and 200-300 nl of virus were infused at a constant low pressure via a pulse generator (WPI) during a time window of 10-20 minutes. After infusion, the capillary was left in place for additional 10 minutes to allow complete diffusion of the virus. For SW experiments, a stainless-steel lancet was inserted via stereotactic apparatus at a depth of -0.5 (from Bregma) and left in place for additional 30 seconds before removal. Animals were allowed to recover and physical conditions carefully monitored daily before euthanize them. All experimental procedures were performed in agreement with the European Union and German guidelines and were approved by the Government of State of Upper Bavaria.

Antibodies and reagents

Western Blot: mouse anti-β actin (1:5000, Sigma), rabbit anti-LC3 (1:1000, Sigma), rabbit anti-iNOS (1:500, Santa Cruz), rabbit anti-Atg7 (1: 500, Abcam), mouse anti-OPA-1 (1:1000, BD Bioscences), mouse anti-Drp1 (1:1000, BD Bioscences), rabbit anti-Ser^{616} phosphorylated Drp1 (1:1000, Cell Signaling), rabbit anti-Ser^{637} phosphorylated Drp1 (1:1000, Cell Signaling), rabbit anti-AMPK (1:1000, Cell Signaling), rabbit anti-AMPK phosphorylated (1:1000, Cell Signaling), mouse anti-

OPA-1 (1:1000, BD Biosciences), mouse anti-Mfn2 (1:1000, Abcam), rabbit anti-TOM20 (1:1000, Santa Cruz), mouse anti-TIM44 (1:1000, BD Biosciences), goat anti-HSP60 (1:1000, Santa Cruz). *Immunostainings:* chicken anti-GFP (1:1000-2000, Aves Labs), rabbit anti-DsRed (1:1000, Rockland), mouse anti-GFAP (1:500, Sigma), rabbit anti-GFAP (1:500, Dako), chicken or mouse anti-GFAP (1:1000, Millipore), rabbit anti-LC3BII (1:300, Cell Signaling), rabbit anti-TOM20 (1:1000 , Santa Cruz), goat anti-HSP60 (1:1000, Santa Cruz), mouse anti-Drp1 (1:1000, BD Bioscences), rabbit anti-Ser^{616} phosphorylated Drp1 (1:1000, Cell Signaling), rabbit anti-Olig2 (1:500, Millipore), rabbit anti-NG2 (1:500, Millipore), rabbit anti-Iba1 (1:500, BD Bioscience), mouse anti-S100β (1:500, Millipore), rabbit anti-Caspase 3-active (1:300, Cell Signaling). *Other reagents:* lipopolysaccharide (1µg/mL, Sigma), mouse recombinant IFN-γ (10 ng/mL, Sigma), mouse recombinant IL-1β (5 ng/mL, GIBCO), mouse recombinant IL-6 (5 ng/mL, Sigma), mouse recombinant TNF-α (20 ng/mL, GIBCO), L-NAME (1mM, Sigma), 1400W (3 µM, Cayman Chemicals), Bafilomycin A1 (100 nM, Invitrogen), MitoSOX (1 µM, Molecular Probes, used according to manufacturer instructions), tetramethylrhodamine ethyl ester (TMRE) (10nM, Molecular Probes).

Viral vectors

Construction of the *G* gene-deleted *GFP*-expressing RABV (SADΔG-GFP) has been described before (Wickersham et al., 2007b). To generate RABV pSADΔG-mitoGFP, a cDNA fragment containing the pre-peptide of human ornithine carbamoyltransferase (5'-ATGCTGAATCTGAGGATCCTGTTAAACAATGCAGCTTTTAGAAATGGTCACAACT TCATGGTTCGAAATTTTCGGTGTGACAACCACTACAAAATTAAAGTGCAGGGGG GATCC-3') fused to the N-terminal of eGFP was cloned into the pSAD T7-

HH_L16_SC, which allows fast and reliable virus rescue (Ghanem et al., 2012). The RABV SADΔG-mitoGFP was amplified in BSR MG-on cells (Finke et al., 2003) complementing the G deficiency of the virus upon induction of G expression by doxycyclin as previously described. Pseutotyping of SADΔG-mitoGFP with EnvA was performed by infection of BHK-EnvARGCD cells, expressing an ASLV-A envelope protein comprising the RABV G cytoplasmic tail at a MOI of 1 as described previously (Wickersham et al., 2007b). Choice of RABV over other viral vectors for delivering *mito-GFP* was determined by (i) the excellent signal-to-noise ratio of fluorescence-based indicators generated by RABV and (ii) the ensuing possibility to perform detailed anatomical measurements (Wickersham et al., 2007a; Wickersham et al., 2007b). Retroviruses (titer of 1-3 x 10^7 particles/ul) or lentiviruses (titer of 1-3 x 10^9 particles/ul) encoding a fluorescent reporter *(GFP* or *Tomato)* and/or *Cre* were used for transducing astrocytes in culture.

Histology and immunostainings

Brain slices. Brains were vibratome sectioned (70µm thick) and slices were permeabilized (0.5% TritonX-100 in PBS) prior overnight incubation with primary antibodies diluted in blocking buffer (3% Bovine Serum Albumin in PBS). Sections were washed with PBS, incubated with appropriate fluorophore-conjugated secondary antibodies (Jackson Immunoresearch) for 2h at room temperature, counterstained with 4',6-diamidino-2-phenylindole (DAPI) and mounted on microscopic slides. *Cultures.* Coverslips were permeabilized with 0.1% TritonX-100 in PBS, incubated overnight at 4^{o}C with primary antibodies diluted in blocking buffer, treated with appropriate fluorophore-conjugated secondary antibodies and mounted on microscopic slides.

Imaging

Time-lapse of astrocytes in culture. Cortical astrocytes grown on glass coverslips were transfected 48h before imaging. Time-lapse imaging was conducted using a Zeiss Observer z1 equipped with a Yokogawa CSU CCD camera and a spinning disc unit. The lasers used had excitation wavelengths of 488 and 540 nm. During acquisition, the laser power and exposure times were kept as lowest as possible to reduce photo-toxicity. Images were acquired using a 63X-1.3NA water immersion objective. Typical experiments were conducted for 8-12h, in which z-stack series were acquired every 3-4 min. For mitochondrial motility experiments, images were acquired for a total duration of 10 min spaced by 30 sec each, in order to track individual mitochondria. Mitochondria (n= 50 per condition from several cells) were tracked off-line by using the ImageJ PlugIn MTrackJ and their motility was defined by the average value of the D2P parameter, which indicates the distance travelled by mitochondria between consecutive frames. Mitochondrial motility was classified in three different groups, using as a threshold value the median length of an astrocyte mitochondrion in the shorter axis (measured as 0.3 µm). Mitochondria were classified as stationary (D2P< 0.3 µm), moving (0.3 µm <D2P< 1 µm) or fast moving (D2P> 1 µm). Average speed was calculated by using MTrackJ.

Time-lapse in brain slices. For live imaging in brain slices, hGFAP-GFP, hGFAP-RFP or hGFAP-TVA mice were used. For imaging of mitochondria, hGFAP-TVA mice at 4 to 7 days after mito-RABV injection were anesthetized with isoflurane, decapitated and the brain was quickly removed into a chilled artificial cerebrospinal fluid (ASCF). Coronal brain slices (250-300µm thick) were prepared using a vibratome (Microm) and maintained at room temperature for 1.5h. Slices were transferred into an imaging chamber mounted on an upright microscope (Olympus BX50WI) equipped with GFP and RFP fluorescence filter sets and a laser-scanning confocal head (Biorad

MRC1024) interfaced with the LaserSharp 2000 software. Experiments were conducted under ACSF perfusion rate of 1.5ml/min (composition in mM: 125 NaCl, 3 KCl, 1.25 NaH_2PO_4, 2 $CaCl_2$, 2 $MgCl_2$, 25 $NaHCO_3$ and 25 D-glucose; pH 7.4) saturated with 95% O_2 and 5% CO_2 and a constant temperature of 30±0.5°C. Imaging of mito-GFP was carried out by using a 60x objective (NA 0.9, Olympus) and an argon laser which intensity was adjusted between 1 and 3% of the maximum power. Time-lapse imaging of mitochondria was obtained by scanning individual astrocytes every 5-10 minutes with an inter-stack interval of 0.5µm and digital zoom of 1.5. Selection of astrocytes for imaging and subsequent analysis was based on their location (cortical layers II/IV), no overt signs of cell damage due to slice cutting (assessed under transmitted and fluorescence light) and stability of mito-GFP signal during baseline recording (30 minutes). For focal application of ACSF, IL-1β dissolved in ACSF (10ng/ml) and LPS+IFNγ (1µg/ml), an extracellular pipette (tip resistance 5-8MΩ; Clark Electromedical Instruments, Reading, UK) was carefully positioned at a distance of ~50µm from the astrocyte avoiding to directly damage any neighboring cell and a constant minimal positive pressure of ~1 psi was maintained for 30 minutes. Pressure and time of treatment were chosen on the basis of the effective area of diffusion of the pipette-containing solution by including Alexa dyes (**Figure S4B-S4C**). Imaging of mitochondria was usually carried out for maximum 2h following positioning of the pipette. Acquired images were subjected to deconvolution (Huygens Professional software; Scientific Volume Imaging, Hilversum, Netherlands) and image alignment (StackReg; http://bigwww.epfl.ch/thevenaz/stackreg) prior analysis, which was performed manually stack-by-stack with ImageJ (National Institutes of Health, Bethesda, United States). To avoid misinterpretations in quantifying fission and fusion events deriving from the potential intrinsic motility of mitochondria, only those organelles which identity could be followed through the

recording time and during at least two consecutives scans were used for analysis. Calculation of fission-fusion indexes were obtained with the following formula after manual labelling of tracked mitochondria: $(E_{FISSION} – E_{FUSION}) / (E_{FISSION} + E_{STABLE} + E_{FUSION})$, in which $E_{FISSION}$ is the number of observed fission events, E_{STABLE} the number of stable events (mitochondria undergoing neither fission nor fusion) and E_{FUSION} the number of observed fusion events.

Imaging software. Image processing was performed with ImageJ (National Institutes of Health, Bethesda, United States) and the final brightness of images was uniformly adjusted with Photoshop (Adobe Systems Incorporated, San Jose, California, United States). Co-localization analysis was performed with the ImageJ Plugin JACoP (NIH). For some analysis and surface rendering, deconvolution processing of confocal acquisitions was performed with the Huygens Professional software (Scientific volume imaging, Hilversum, Netherlands).

Evaluation of apoptosis and necrosis

Apoptotic and necrotic events in wild-type astrocytes were determined by flow cytometry (Guava EasyCyte Mini, Guava Technologies,Hayward, CA), using the Guava Nexin reagent (Guava Technologies,Hayward, CA) as previously reported (Angeloni et al., 2011). Guava Nexin reagent contains annexin V- phycoerythrin (PE), that detects the residues of phosphatidylserine on the external membrane of apoptotic cells, and the cell impermeant dye 7-amino-actinomycin D (7-AAD), to discriminate dead ones. Astrocytes analyzed at different time-points were trypsinyzed and resuspended in equal amounts of PBS and Guava Nexin Reagent. Cells were stained for 20’ at room temperature in the dark before measurements were taken. For evaluation of apoptosis in Atg7 floxed astrocytes, immunostaining for Caspase 3-

active (Cell Signalling) was carried out in coverslips treated with control or Cre-expressing lentivirus and stimulated with LPS+IFNγ for 1, 3 and 8 days.

ATP assay

Cellular steady state ATP levels were measured using the luciferase-based ATP Bioluminescence assay kit HS II (Roche Applied Science), according to the manufacturer's instructions. Astrocytes were treated for the given time-points and, where indicated, medium was replaced with a 1mM glucose medium (low glucose) 24h before harvesting the cells. Bioluminescence, indicative of the ATP content, was measured using a LB96V luminometer (Berthold Technologies) and normalized to total protein levels.

Oxygen consumption

Respiration was measured using the XF96 analyzer (Seahorse Bioscience)(Ferrick et al., 2008). Briefly, 30,000 cells per well were seeded in 1 mM Glucose medium 24h before performing the measurements. The oxygen consumption rate (OCR) was then quantified after sequential addition of 2 µM Oligomycin, 1 µM FCCP and 5 µM Rotenone/Antimycin A, as previously published (Brand and Nicholls; Ferrick et al., 2008).

Mitochondrial ROS evaluation

Mitochondrial ROS production was evaluated by incubating astrocytes at 37°C with the live-cell permeant indicator MitoSOX Red (Molecular Probes, used according to manufacturer instructions). MitoSOX (1 µM) was added to the cell medium for 10 minutes, after which cells (kept in dark) were washed twice in warm buffer (HBSS) before live imaging of multiple cells (usually 10-20 per dish) during a time-window of

30 minutes. After imaging (514nm/560nm), samples were fixed in PFA 4% for 10 minutes on the microscope stage and subjected to immunostainings at 37°C in dark (1h incubation with primary antibodies plus 1h incubation with secondary antibodies). Normalization of MitoSOX fluorescence on Tom20 immunoreactivity was performed with ImageJ.

Western blot

Cells were scraped off in ice-cold PBS and lysed in CelLytic plus protease (1:500) and/ or phosphatase (1:100) inhibitor cocktail. After centrifugation at 12000 rpm (4˚C) for removal of cellular debris, proteins were separated by SDS-PAGE and transferred to nitrocellulose membranes using standard procedures. After blocking unspecific sites, the membranes were incubated overnight at 4°C with antibodies recognizing the proteins of interest. Detection was performed after 60 min incubation with secondary antibodies conjugated to horseradish peroxidase (Promega) and subsequent conversion with a chemiluminescent substrate (GE-Healthcare).

Electron microscopy

Primary cortical astrocytes were plated in poly-L-lysine (0.01%, Sigma)-coated glass slides (LabTek Chamber Slides) at a density of 100,000 cells per slide (area = 1.8 cm2) and treated for 8 or 24h with LPS+IFNγ or vehicle. Samples were fixed 2 hours in 2.5% glutaraldehyde (Electron Microscopy Sciences) dissolved in 0.1 M phosphate buffer (PB, pH 7.4). Astrocytes were then post-fixed for 1 hour in 1% osmium tetroxide (Electron Microscopy Sciences) in PB, and stained with ethanol 70% containing 1% uranyl acetate (Sigma). After sample dehydration in graded alcohol series and embedding in Epon (Sigma), ultrathin sections (with silver to gray interference) were cut with a diamond knife (Diatome), mounted on Formvar-coated

single slot grids and then counterstained with 3% uranyl acetate and with lead citrate (0.2%, Sigma). Sections were visualized using a Philips CM100 transmission electron microscope. The density of autophagic vacuoles was then determined by counting the number of organelles per astrocyte per μm^2, while analysis of cristae was performed on high magnifications images (24,500 X) counting the number of cristae per unit of mitochondrial surface.

Supplemental figure legends

Figure S1. Specificity of EnvA-pseudotyped mito-RABV in targeting TVA-expressing astrocytes and absence of visible mitochondrial dysfunction following transduction. (A) Rabies virus construct (SADΔG) used for expressing *mito-GFP in vivo* (mito-RABV). **(B)** Representative confocal picture showing mito-GFP expressing cortical cells immunoreactive for the astrocyte marker S100β. High magnification and orthogonal views of the boxed area are shown. Bar 80 µm. **(C)** Representative confocal picture showing mito-GFP expressing cortical cells being negative for pan-non-astrocytic markers, including microglial (Iba1) and oligodendroglial lineage markers (NG2 and Olig2). Bar 80 µm. **(D)** *In vivo* dual targeting of hGFAP-TVA astrocytes by co-injecting EnvA-pseudotyped mito-RABV and mCherry-RABV. **(E)** Example of a single astrocyte co-expressing mCherry (revealing the entire morphology of the cell) and mito-GFP *in vivo*. Insets show mitochondria entering the finest mCherry+ astrocytic processes (arrowheads). Bar 10 µm. **(F)** Assessment of mitochondrial morphology and membrane potential in mito-RABV transduced astrocytes revealed that low titre virus (~10^{-6}) did not visibly affect their physiology. Example of an astrocyte in culture (arrowheads) at 5 days after transduction with mito-RABV. The sample was imaged live by confocal microscopy 30 minutes after incubation with 10 nM TMRE (tetramethylrhodamine ethyl ester), which intensity reflects the mitochondrial membrane potential. Pictures show the single and merged channels of mito-GFP and TMRE. Bar 10 µm. **(G)** Linescan shown TMRE fluorescence intensity along the dashed line depicted in **F**. The segment crossing the mito-RABV transduced astrocyte is highlighted in green. **(H)**

Quantification of the average TMRE signal intensity per astrocyte at 5 and 10 days following mito-RABV transduction (n= at least 5 cells per condition).

Figure S2. Perineuronal distribution of astrocytic mitochondria *in vivo*. (A) Rabies virus constructs used for targeting specifically *mito-GFP* to astrocytes (EnvA-pseudotyped mito-RABV) and cytosolic *mCherry* to neurons (G-pseudotyped mCherry-RABV) in hGFAP-*TVA* mice *in vivo*. **(B)** Scheme of virus delivery in the cortex of hGFAP-*TVA* mice and expected outcome. **(C)** Example showing a single mito-RABV transduced astrocyte contacting a mCherry-expressing pyramidal neuron in layers II/III at 7dpi. **(D)** 3D front and back views of the area boxed in **C**. Note the spatial allocation of astrocytic mitochondria around the soma and dendrites of the neuron (arrowheads). **(E)** Example of a mito-RABV transduced astrocyte contacting an interneuron in layers II/III. **(F)** 3D front and back views of the area boxed in **E**. Bars 30 µm.

Figure S3. Induction of reactive astrogliosis following cortical SW. (A) Confocal acquisitions depicting the immunoreactivity for GFAP, Iba1 (microglia) and CD45 (invading leukocytes) in the intact cortex, following saline infusion or following SW with or without infusion of a lentivirus encoding *GFP* under the hGFAP promoter (to target astrocytes). Note the substantial induction of gliosis (GFAP immunoreactivity) at 4 days after SW in the penumbra and the invasion of pro-inflammatory cells in the lesion core. A similar pattern of GFAP and CD45 immunoreactivity was induced with or without injection of virus. Bars 100 µm. **(B)** Experimental timeline for assessing mitochondrial morphology in astrocytes of hGFAP-*TVA* mice following SW and mito-RABV infusion. **(C)** Confocal acquisitions showing the pattern of immunoreactivity for GFAP and CD45 in the cortex of mito-RABV injected mice subjected to SW at

different time points. Panels on the right depict examples of individual mito-RABV transduced astrocytes located in the penumbra (GFAP+) or lesion core (GFAP-) and the appearance of their nuclei (revealed with DAPI staining). Bars 100 and 10 µm.

Figure S4. Lesion core astrocytes are surrounded by a local pro-inflammatory environment. (A) High magnifications of mito-RABV transduced astrocytes (yellow arrowheads) in the lesion core at 4dpi showing the close proximity of several CD45+ pro-inflammatory cells (white arrowheads). Note the uniform DAPI staining in astrocytes and the characteristic fragmentation of their mitochondria. Bar 20 µm. **(B)** Validation of local drug infusion in acute brain slices. Cortical slices were obtained from hGFAP-RFP mice and an extracellular pipette containing IL-1β and Alexa488 was positioned in proximity of a selected RFP+ astrocyte (30-50 µm of distance). At the minimal ejection pressure of 1 psi, the diffusion radius of Alexa488 was then measured at regular intervals of time, in order to define the astrocyte's branches proximal (within the radius) or distal (outside the radius) from the releasing pipette as shown in **C**. Accordingly, the maximal distance (~40 µm) of IL-1β + Alexa488 diffusion measured at 30' after infusion was utilized as a parameter to define branches within quadrant I during analysis of mitochondrial dynamics in mito-RABV transduced astrocytes. Bars 20 and 10 µm. **(D)** Z-stack projection of a confocal acquisition showing a single GFP+ astrocyte within an acute cortical slice obtained from hGFAP-GFP mice. After 30 minutes of baseline recording (10 minutes/frame), IL-1β was slowly infused by placing an extracellular pipette in the top-left corner. The GFP signal intensity of branches within the proximal and distal areas to the pipette was analyzed off-line through 90 minutes of imaging, to detect signs of cellular alteration or process pruning. Bar 10 µm. **(E)** Time-lapse sequence of selected

frames (single stacks, in pseudocolors) of the proximal and distal areas boxed in **D** starting from 30 minutes prior to 90 minutes after IL-1β application. Bar 10 µm. **(F)** Diagram showing the average fluorescence intensity of the circular ROIs (3 for each area) distributed along the selected astrocytic processes as shown in **E** and normalized to the initial value at time -30 minutes.

Figure S5. Analysis of astrocyte viability and bioenergetics following pro-inflammatory stimulation. (A) Average mitochondrial length measured in astrocytes following treatment for 4 or 24h with different pro-inflammatory cytokines compared to controls. (n=3 cells per condition, 15-20 mitochondria/cell; ***, $p < 0.001$). **(B)** Cytofluorimetric analysis of control cortical astrocytes and astrocytes treated with LPS+IFNγ for 24 or 48h and stained for Annexin V and 7-AAD (2,000 events per condition). **(C)** Quantification of the proportion of apoptotic or dead astrocytes in absence or following stimulation (n=3 independent experiments). **(D)** ATP measurements in astrocytes subjected to the indicated treatments. With high glucose medium, ATP production is quickly increased following LPS+IFNγ stimulation. Under low glucose medium, the same treatment fails in inducing such an increase in ATP production (n= 3 experiments). **(E)** Example of oxygen consumption rate (OCR) curve obtained with SeaHorse (XF96 Analyzer, SeaHorse Bioscience). OCR is measured after sequential addition of mitochondrial stressors, and the bioenergetic capacity of mitochondria under basal conditions (basal respiration), maximal uncontrolled respiration (maximal respiratory capacity) and increased energy demand (spare respiratory capacity) is calculated from the areas under the curve between corresponding treatments.

Figure S6. Drp1 mediates mitochondrial fragmentation following astrocyte stimulation with LPS+IFNγ. **(A)** Immunostaining for total Drp1 and the mitochondrial marker Hsp60 performed at different time points after treatment. Note the up-regulation of Drp1 following stimulation. Bar 5 µm. **(B)** Confocal pictures showing the localization of Drp1 on mitochondria of mito-RABV transduced astrocytes in control and SW injured hGFAP-TVA mice *in vivo*. Note the localization of Drp1+ punctae at the points of mitochondrial fission in reactive astrocytes. Bar 10 µm. **(C, D)** Knock-down of Drp1. Constructs encoding for GFP and miR-scramble or miR-Drp1 were used to transfect astrocytes 3-5 days prior immunostaining. Panels show single and merged channels. Bars 10 µm. **(E, F)** Blockade of Drp1 activation prevents mitochondrial fragmentation in stimulated astrocytes. Astrocytes were transfected with a construct encoding for YFP alone **(E)** or YFP and the dominant negative form of Drp1 (K38E) **(F)** and mitochondrial morphology evaluated by immunostaining for Tom20. Insets show high magnifications of the boxed areas. Although Drp1 (K38E) induces a modest hyperelongation of the mitochondrial network, it prevents mitochondrial fragmentation following stimulation at 4h. Bars 15 µm.

Figure S7. Pharmacological inhibition of iNOS prevents LPS+IFNγ-mediated astrocyte mitochondrial fission in brain slices. **(A)** Scheme depicting the experimental approach to assess the requirement for iNOS activity (leading to NO production) during focal application of LPS+IFNγ in mito-RABV transduced astrocytes in slices. **(B)** Example of mitochondrial dynamics occurring within the proximal branches (boxed area) during focal application of LPS+IFNγ. Lower panels show selected time-lapse frames of the boxed area illustrating the prevalence of fission events. Bars 10µm. **(C)** Index of fission-fusion for each quadrant and for whole

astrocytes during LPS+IFNγ application (n=5 cells; **, p< 0.01). **(D)** Example of mitochondrial dynamics occurring within the proximal branches during focal application of LPS+IFNγ and bath application of L-NAME starting from 30' before the experiment. Lower panels show selected time-lapse frames of the boxed area illustrating lack of significant mitochondrial fission. Bars 10µm. **(E)** Index of fission-fusion for each quadrant and for whole astrocytes during LPS+IFNγ and L-NAME co-application (n=5 cells).

Figure S8. Induction of autophagy following stimulation with pro-inflammatory mediators. (A) Immunoblot showing a time course analysis of LC3B-II (the autophagosomal-associated isoform) in astrocytes after treatment with LPS+IFNγ. **(B)** Immunoblot showing the increase in LC3B-II in astrocytes at 8h after treatment with the indicated pro-inflammatory cytokines. **(C)** Quantification of GFP+ autophagosomes during time-lapse experiments in astrocytes expressing *GFP-LC3* and following treatment with LPS+IFNγ (n=6-7 cells/condition). **(D, E)** Examples of time-lapse imaging of a control **(D)** and a LPS+IFNγ treated astrocyte **(E)** co-transfected with *mito-DsRed* and *GFP-LC3* to monitor the temporal evolution of mitochondrial rearrangements and autophagosome formation during 10h of imaging. Bars 10 µm. **(F)** Magnifications of the areas boxed in **D** and **E** (1-1' and 2-2') displaying the superimposition between mito-DsRed and GFP-LC3. Arrowheads point to autophagosomes localized on mitochondria. Bar 3 µm. **(G)** Evaluation of the autophagic flux using the dual colour reporter DsRed-LC3-GFP, which contains the Atg4 protease-specific recognition site between LC3 and GFP domains and thus allows for monitoring autophagic activity (Sheen et al., 2011). Pictures show control or LPS+IFNγ treated astrocytes expressing the reporter construct. Bottom panels

show zooms depicting the appearance of DsRed+ autophagosomes, indicatibe of autophagy. Presence or absence of GFP indicates phagophores/early autophagosomes (GFP+/DsRed+) or late autophagosomes/lysosomes (GFP-/DsRed+). **(H)** Quantification of DsRed-only+ (red bars) and DsRed+/GFP+ punctae (green bars) per astrocyte under the indicated conditions illustrate the extent of autophagic flux (n=8-15 cells/condition).

Figure S9. Time-dependent co-localization of mitochondria with lysosomal markers following astrocyte stimulation. (A) Confocal pictures of individual astrocytes transfected with *mito-GFP* and treated with LPS+IFNγ for 4 or 24h. Lower panels show enlargements of the boxed areas reporting on the expression and distribution of the late-endosome marker Rab7. Arrowheads point to single mitochondria. Lower graphs show the intensity profile of mito-GFP and Rab7 for selected mitochondria (circled in the upper images). Bars 10 and 5 µm. **(B)** Quantification of the co-localization between mito-GFP and Rab7 or Lamp2 at 4 and 24h following stimulation (n=5 cells/time point; *, $p< 0.05$; **, $p< 0.01$). **(C)** Confocal pictures of control and stimulated astrocytes transfected with *mito-GFP* depicting the expression and distribution of LC3B-II and Lamp2. While at 4h many mitochondria co-localize with LC3B-II, at 24h there is a significant co-localization only with Lamp2. Arrowheads point to single mitochondria. Lower graphs show the line-scan profile of mito-GFP, LC3B-II and Lamp2 corresponding to each analyzed condition. Bars 20 and 5 µm. **(D)** Example of non-transfected astrocyte stimulated for 24h and analyzed as in **C**. Co-localization between the mitochondrial marker Tom20 and Lamp2 is shown. Bars 10 and 5 µm.

Figure S10. Atg7 deletion in astrocytes exposed to LPS+IFNγ prevents induction of autophagy. (A) Western blot evaluation of Atg7 protein loss in cultured astrocytes exposed to control or Cre-expressing viruses for 5-7 days. **(B)** Western blot evaluation of LC3B conversion in $Atg7^{lox/lox}$ astrocytes upon Cre expression and treatment with LPS+IFNγ for 4h. **(C)** Atg7-deficient astrocytes fail in up-regulating LC3B-II following stimulation with LPS+IFNγ. Bars 30 and 5 µm. **(D)** Assessment of Drp1 and its phosphorylated form at Ser-637 in $Atg7^{lox/lox}$ astrocytes exposed to LPS+IFNγ. Note the clear up-regulation of P-Drp1 (Ser-637) in Cre-transduced astrocytes, which correlates well with the observed mitochondrial hyperfusion (Cribbs and Strack, 2007; Gomes et al., 2011). **(E)** Electron micrographs of stimulated $Atg7^{lox/lox}$ astrocytes showing the drastic reduction of autophagic vacuoles in knockout cells. Arrowheads point to autophagic vacuoles in CTRL virus-transduced astrocytes. Bars 10 and 1 µm. **(F)** Quantification of autophagic vacuoles in control virus or Cre-transduced $Atg7^{lox/lox}$ astrocytes at 24h after LPS+IFNγ stimulation (n = 5 cells; **, $p < 0.01$). **(G)** Examples showing the densitiy of cristae in mitochondria of wilt-type or $Atg7^{lox/lox}$ astrocytes following the indicated treatments. Bars 0.5 µm. **(H)** Quantification of cristae density for the conditions shown in **G** (n = 40-60 fields and at least 70 mitochondria per condition; ***, $p < 0.001$). **(I)** Interfering with Atg4B prevents mitochondrial network restoration. Astrocytes were transfected with a mCherry-encoding plasmid for the dominant negative form of Atg4 (C74A) and mitochondrial morphology assessed following stimulation with LPS+IFNγ. By 24h, clusters of hyperfused mitochondria became visible in transfected astrocytes. Bars 5 µm. **(J)** Quantification of mitochondrial morphology in astrocytes transfected with control of Atg4(C74A) vectors and subjected to LPS+IFNγ stimulation (n=3 experiments, 50-100 cells).

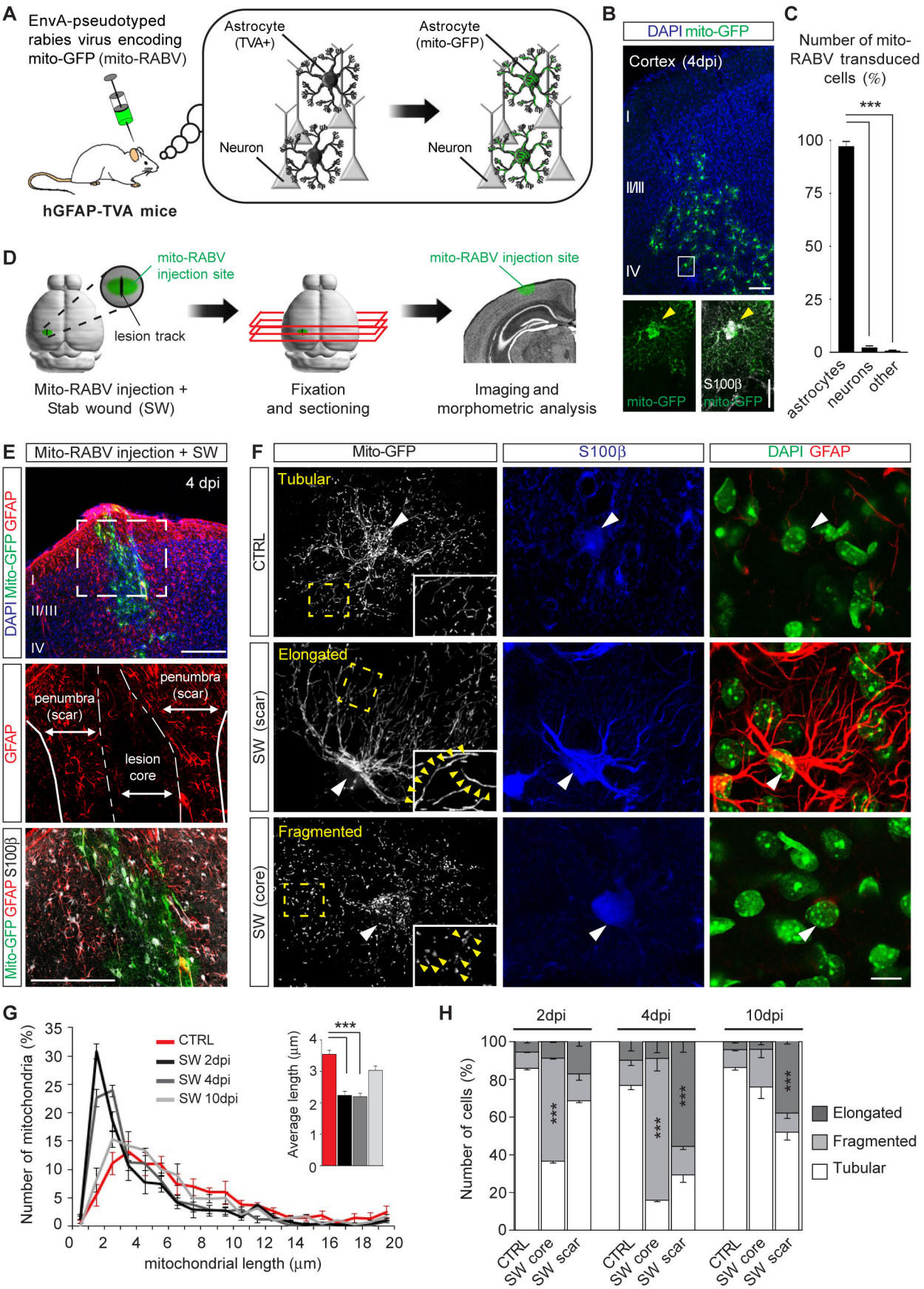
A
EnvA-pseudotyped rabies virus encoding mito-GFP (mito-RABV)
hGFAP-TVA mice
Astrocyte (TVA+)
Neuron
Astrocyte (mito-GFP)
Neuron
B
DAPI mito-GFP
Cortex (4dpi)
I
II/III
IV
mito-GFP
S100β
mito-GFP
C
Number of mito-RABV transduced cells (%)
***
100
75
50
25
0
astrocytes
neurons
other
D
mito-RABV injection site
lesion track
Mito-RABV injection + Stab wound (SW)
Fixation and sectioning
mito-RABV injection site
Imaging and morphometric analysis
E
Mito-RABV injection + SW
4 dpi
DAPI Mito-GFP GFAP
GFAP
penumbra (scar)
penumbra (scar)
lesion core
Mito-GFP GFAP S100β
F
Mito-GFP
S100β
DAPI GFAP
CTRL
Tubular
SW (scar)
Elongated
SW (core)
Fragmented
G
Number of mitochondria (%)
CTRL
SW 2dpi
SW 4dpi
SW 10dpi
mitochondrial length (μm)
Average length (μm)
***
H
2dpi
4dpi
10dpi
Number of cells (%)
Elongated
Fragmented
Tubular
CTRL
SW core
SW scar

Figure 1

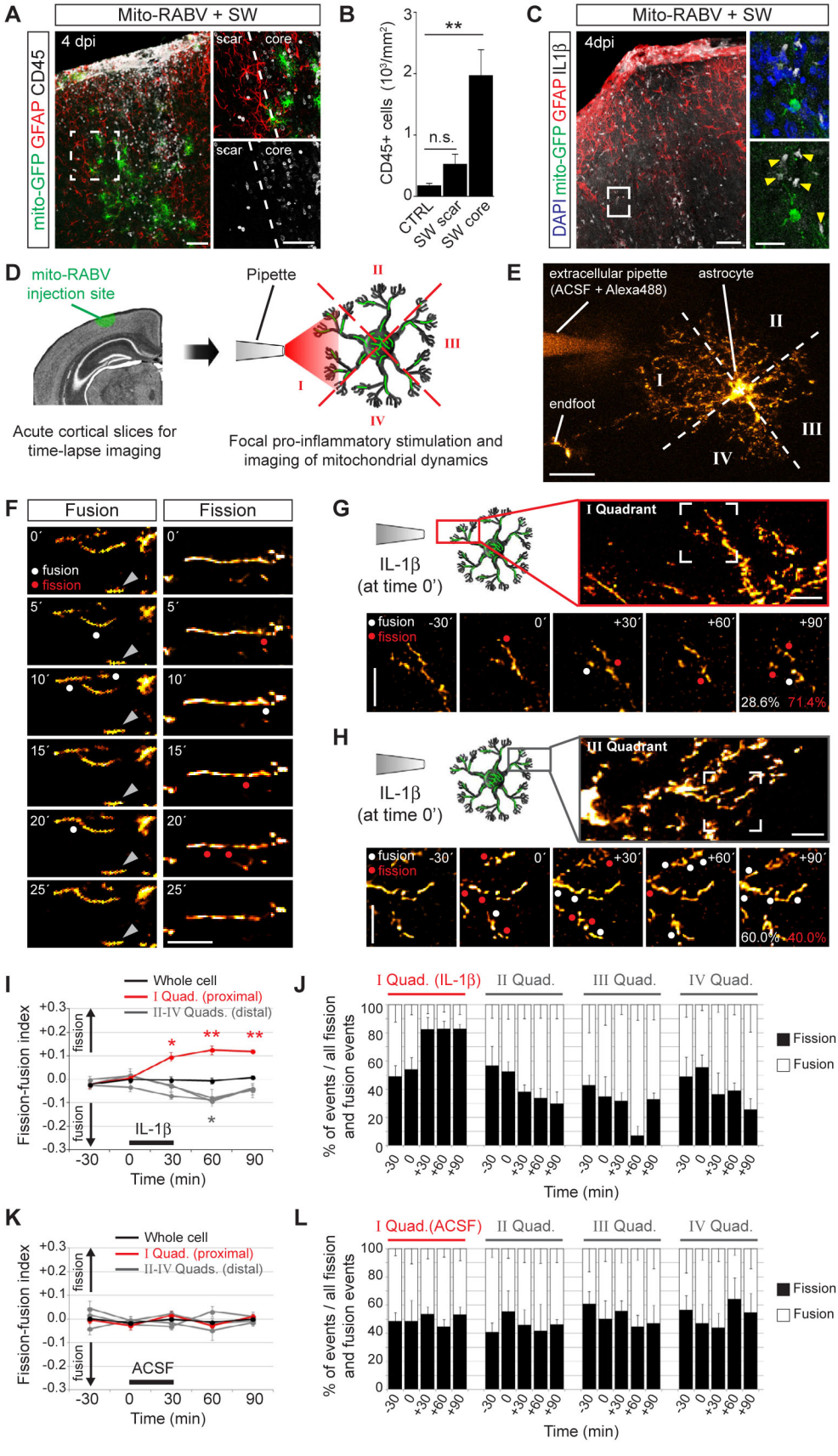
A
Mito-RABV + SW
4 dpi
scar
core
mito-GFP GFAP CD45
B
CD45+ cells (10³/mm²)
**
n.s.
CTRL
SW scar
SW core
C
Mito-RABV + SW
4dpi
DAPI mito-GFP GFAP IL1β
D
mito-RABV injection site
Pipette
Acute cortical slices for time-lapse imaging
Focal pro-inflammatory stimulation and imaging of mitochondrial dynamics
E
extracellular pipette (ACSF + Alexa488)
astrocyte
endfoot
F
Fusion
Fission
fusion
fission
G
IL-1β (at time 0')
I Quadrant
28.6%
71.4%
H
II Quadrant
60.0%
40.0%
I
Whole cell
I Quad. (proximal)
II-IV Quads. (distal)
Fission-fusion index
IL-1β
Time (min)
J
I Quad. (IL-1β)
II Quad.
III Quad.
IV Quad.
% of events / all fission and fusion events
Fission
Fusion
Time (min)
K
ACSF
L
I Quad.(ACSF)

Figure 2

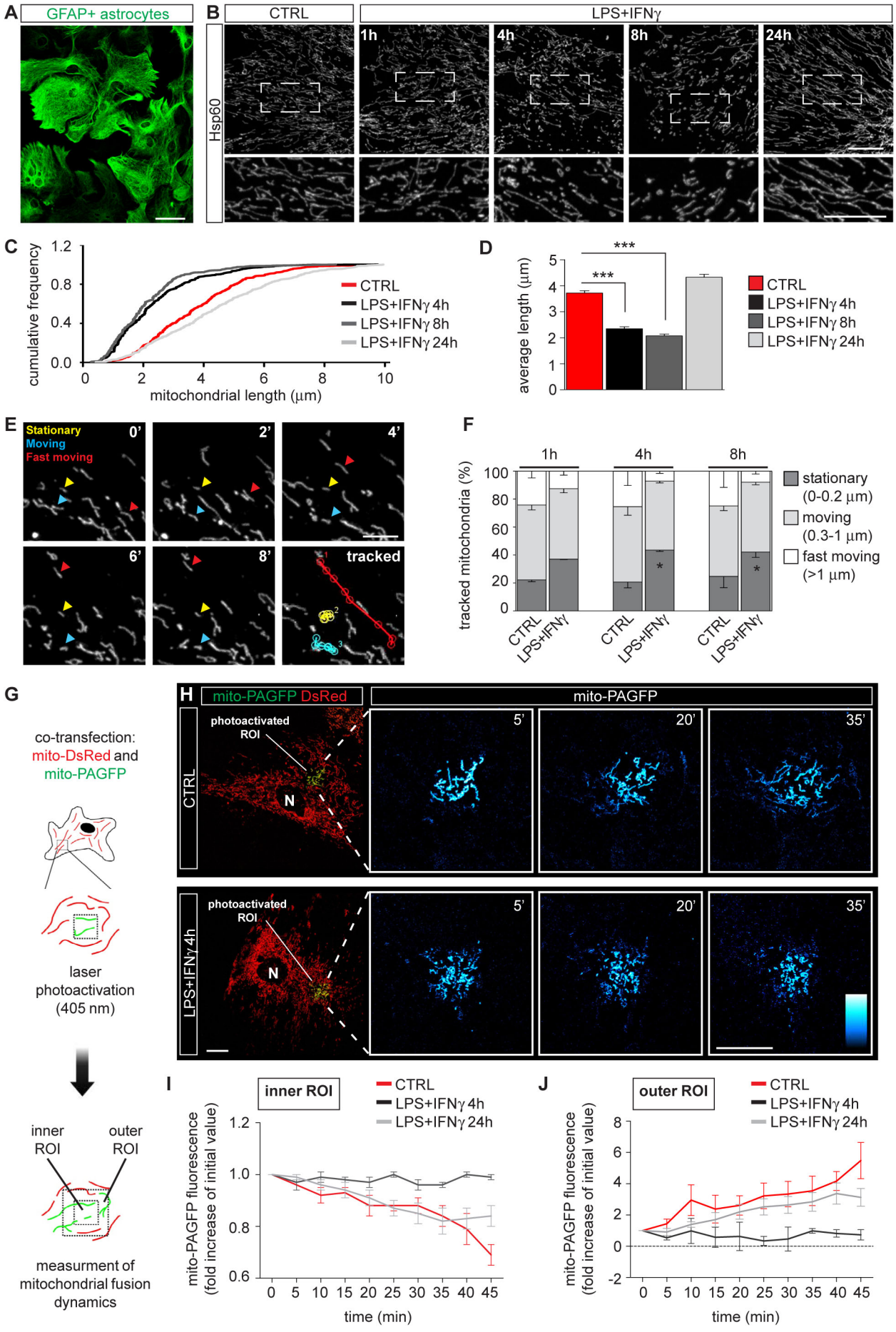
A
GFAP+ astrocytes
B
CTRL
LPS+IFNγ
1h
4h
8h
24h
Hsp60
C
cumulative frequency
1.2
0.8
0.4
0.0
0
2
4
6
8
10
mitochondrial length (μm)
CTRL
LPS+IFNγ 4h
LPS+IFNγ 8h
LPS+IFNγ 24h
D
average length (μm)
5
4
3
2
1
0
***
***
CTRL
LPS+IFNγ 4h
LPS+IFNγ 8h
LPS+IFNγ 24h
E
Stationary
Moving
Fast moving
0'
2'
4'
6'
8'
tracked
F
1h
4h
8h
tracked mitochondria (%)
100
80
60
40
20
0
CTRL
LPS+IFNγ
stationary (0-0.2 μm)
moving (0.3-1 μm)
fast moving (>1 μm)
G
co-transfection:
mito-DsRed and
mito-PAGFP
laser
photoactivation
(405 nm)
inner ROI
outer ROI
measurment of
mitochondrial fusion
dynamics
H
mito-PAGFP DsRed
mito-PAGFP
CTRL
LPS+IFNγ 4h
photoactivated ROI
N
5'
20'
35'
I
inner ROI
CTRL
LPS+IFNγ 4h
LPS+IFNγ 24h
mito-PAGFP fluorescence (fold increase of initial value)
1.2
1.0
0.8
0.6
0
5
10
15
20
25
30
35
40
45
time (min)
J
outer ROI
CTRL
LPS+IFNγ 4h
LPS+IFNγ 24h
mito-PAGFP fluorescence (fold increase of initial value)
8
6
4
2
0
-2
0
5
10
15
20
25
30
35
40
45
time (min)

Figure 3

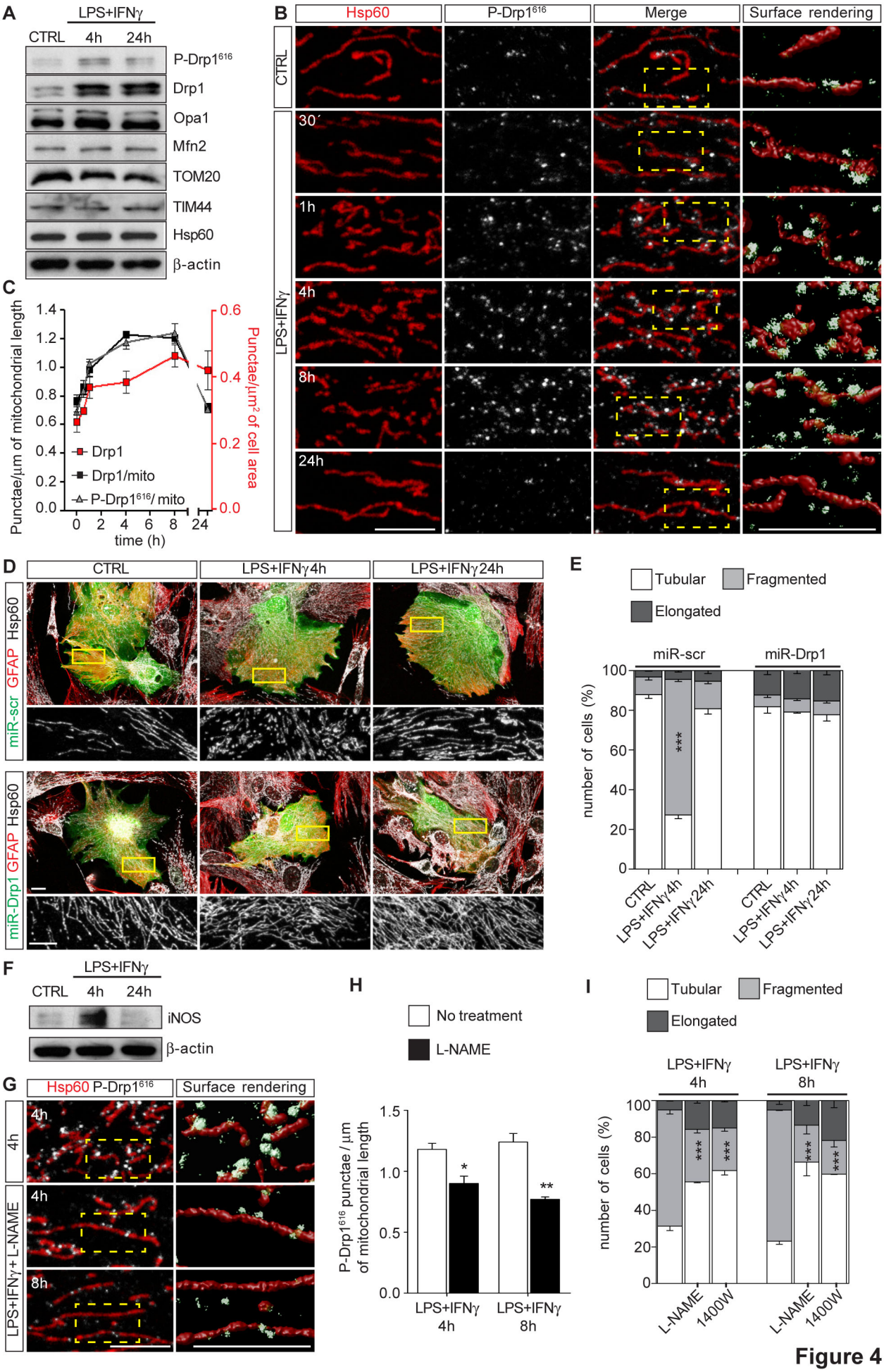
A
LPS+IFNγ
CTRL
4h
24h
P-Drp1616
Drp1
Opa1
Mfn2
TOM20
TIM44
Hsp60
β-actin
B
Hsp60
P-Drp1616
Merge
Surface rendering
CTRL
LPS+IFNγ
30´
1h
4h
8h
24h
C
Punctae/µm of mitochondrial length
Punctae/µm2 of cell area
Drp1
Drp1/mito
P-Drp1616/ mito
time (h)
D
CTRL
LPS+IFNγ4h
LPS+IFNγ24h
miR-scr GFAP Hsp60
miR-Drp1 GFAP Hsp60
E
Tubular
Fragmented
Elongated
miR-scr
miR-Drp1
number of cells (%)
CTRL
LPS+IFNγ4h
LPS+IFNγ24h
F
LPS+IFNγ
CTRL
4h
24h
iNOS
β-actin
G
Hsp60 P-Drp1616
Surface rendering
4h
LPS+IFNγ+ L-NAME
8h
H
No treatment
L-NAME
P-Drp1616 punctae / µm of mitochondrial length
LPS+IFNγ 4h
LPS+IFNγ 8h
I
Tubular
Fragmented
Elongated
LPS+IFNγ 4h
LPS+IFNγ 8h
number of cells (%)
L-NAME
1400W

Figure 4

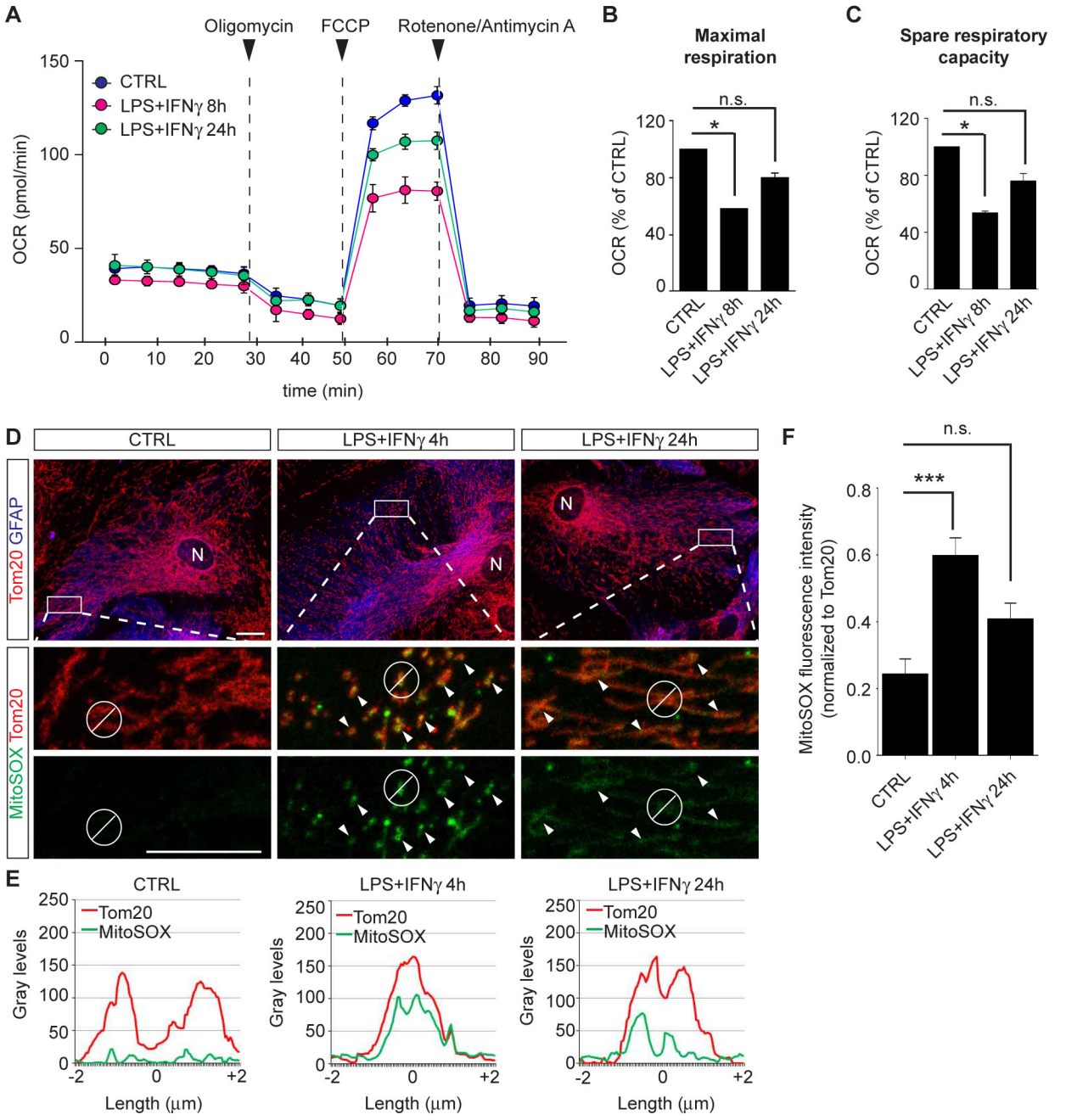
A
Oligomycin
FCCP
Rotenone/Antimycin A
CTRL
LPS+IFNγ 8h
LPS+IFNγ 24h
OCR (pmol/min)
time (min)
B
Maximal respiration
OCR (% of CTRL)
n.s.
*
C
Spare respiratory capacity
D
CTRL
LPS+IFNγ 4h
LPS+IFNγ 24h
Tom20 GFAP
MitoSOX Tom20
N
E
Tom20
MitoSOX
Gray levels
Length (μm)
F
MitoSOX fluorescence intensity (normalized to Tom20)
***

Figure 5

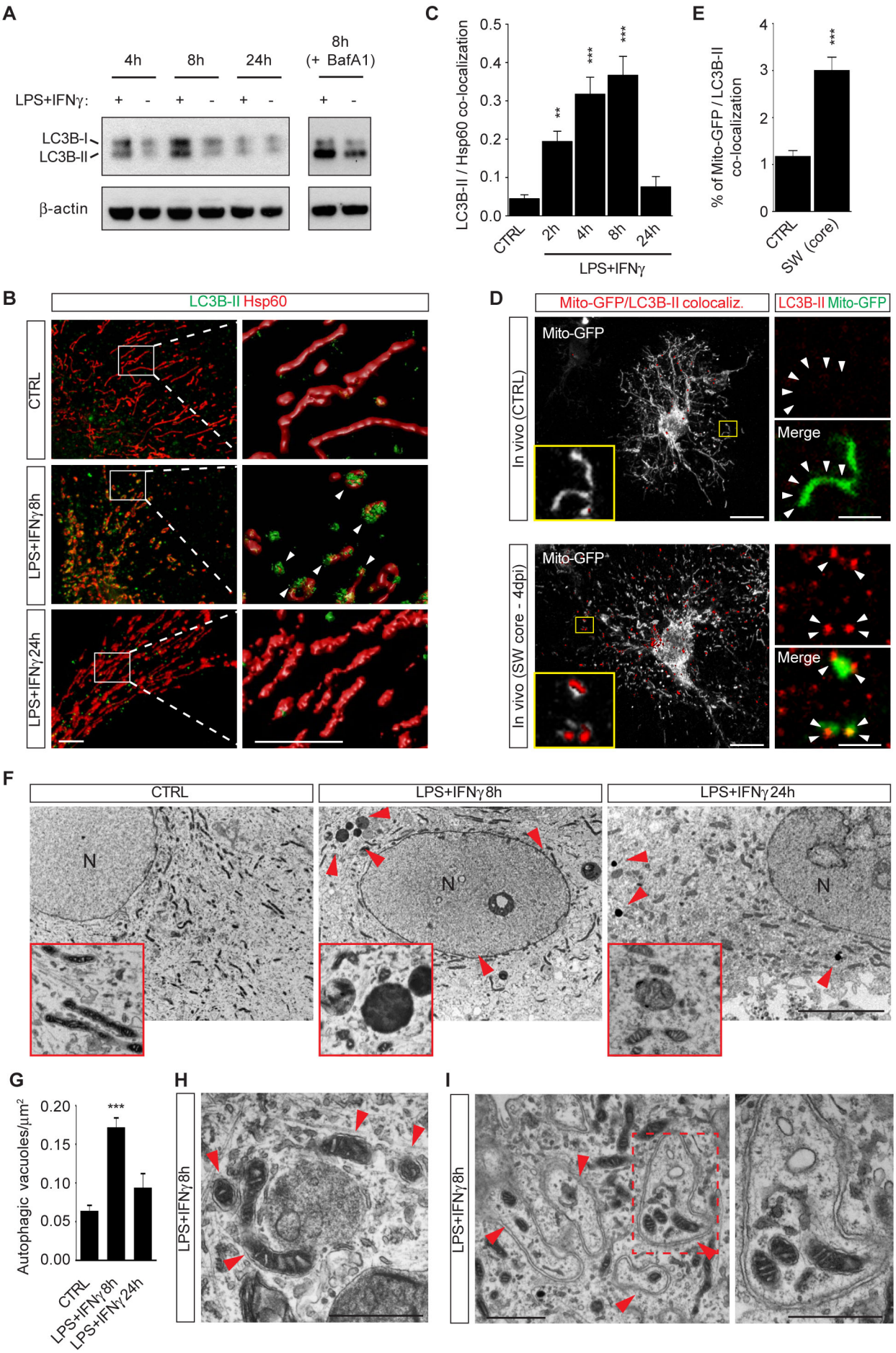
A
4h
8h
24h
8h
(+ BafA1)
LPS+IFNγ:
+ - + - + - + -
LC3B-I
LC3B-II
β-actin
C
LC3B-II / Hsp60 co-localization
0.5
0.4
0.3
0.2
0.1
0.0
**
***
***
CTRL
2h
4h
8h
24h
LPS+IFNγ
E
% of Mito-GFP / LC3B-II co-localization
4
3
2
1
0
***
CTRL
SW (core)
B
LC3B-II Hsp60
CTRL
LPS+IFNγ8h
LPS+IFNγ24h
D
Mito-GFP/LC3B-II colocaliz.
LC3B-II Mito-GFP
In vivo (CTRL)
Mito-GFP
Merge
In vivo (SW core - 4dpi)
Mito-GFP
Merge
F
CTRL
LPS+IFNγ8h
LPS+IFNγ24h
N
N°
N
G
Autophagic vacuoles/µm²
0.20
0.15
0.10
0.05
0.00
***
CTRL
LPS+IFNγ8h
LPS+IFNγ24h
H
LPS+IFNγ8h
I
LPS+IFNγ8h

Figure 6

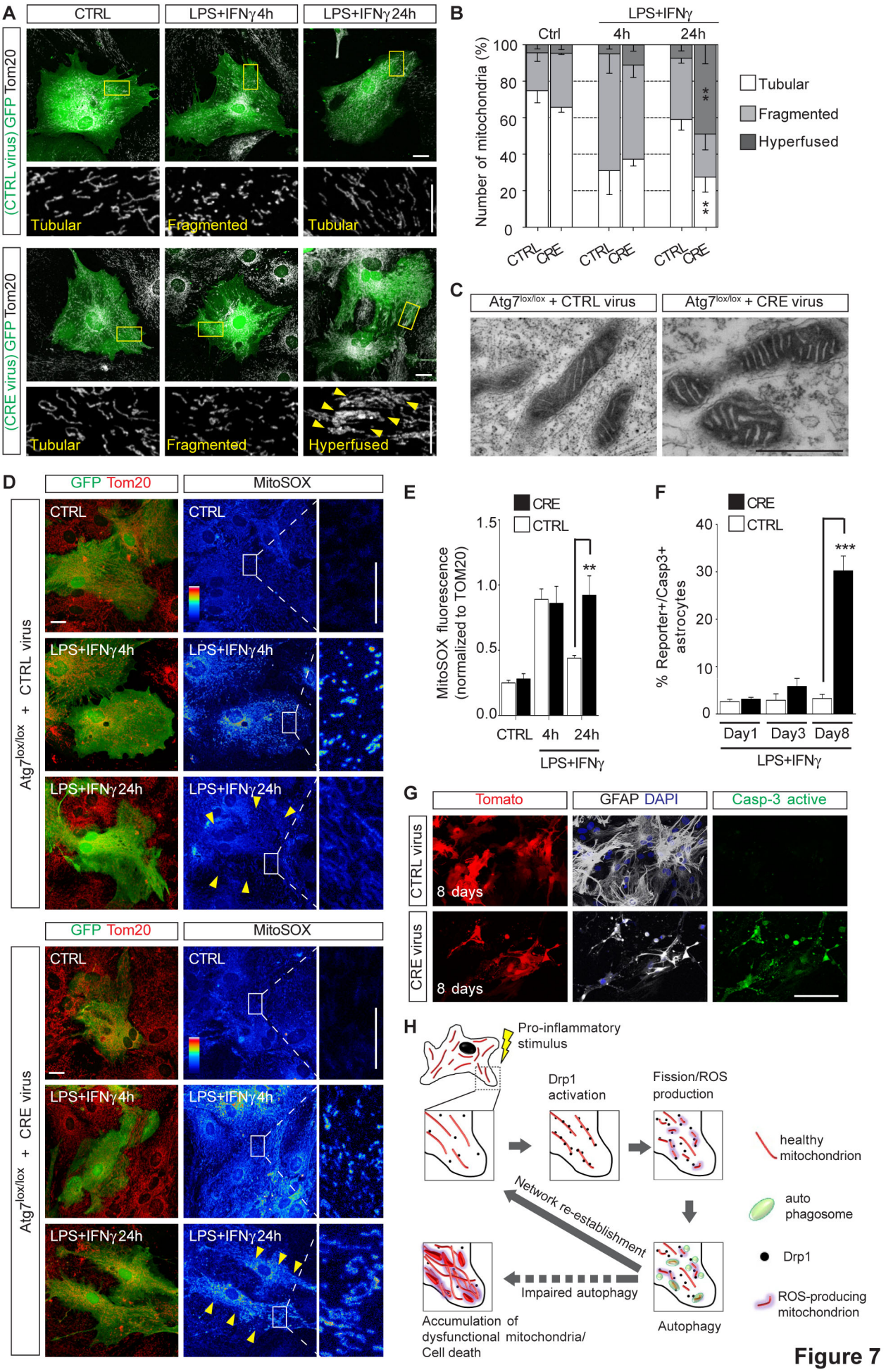
A
CTRL
LPS+IFNγ4h
LPS+IFNγ24h
(CTRL virus) GFP Tom20
(CRE virus) GFP Tom20
Tubular
Fragmented
Tubular
Tubular
Fragmented
Hyperfused
B
LPS+IFNγ
Ctrl
4h
24h
Number of mitochondria (%)
100
80
60
40
20
0
Tubular
Fragmented
Hyperfused
**
**
CTRL
CRE
CTRL
CRE
CTRL
CRE
C
Atg7lox/lox + CTRL virus
Atg7lox/lox + CRE virus
D
GFP Tom20
MitoSOX
Atg7lox/lox + CTRL virus
CTRL
LPS+IFNγ4h
LPS+IFNγ24h
Atg7lox/lox + CRE virus
E
CRE
CTRL
MitoSOX fluorescence (normalized to TOM20)
1.5
1.0
0.5
0.0
**
CTRL
4h
24h
LPS+IFNγ
F
CRE
CTRL
% Reporter+/Casp3+ astrocytes
40
30
20
10
0
***
Day1
Day3
Day8
LPS+IFNγ
G
Tomato
GFAP DAPI
Casp-3 active
CTRL virus
CRE virus
8 days
8 days
H
Pro-inflammatory stimulus
Drp1 activation
Fission/ROS production
Network re-establishment
Impaired autophagy
Accumulation of dysfunctional mitochondria/ Cell death
Autophagy
healthy mitochondrion
auto phagosome
Drp1
ROS-producing mitochondrion

Figure 7

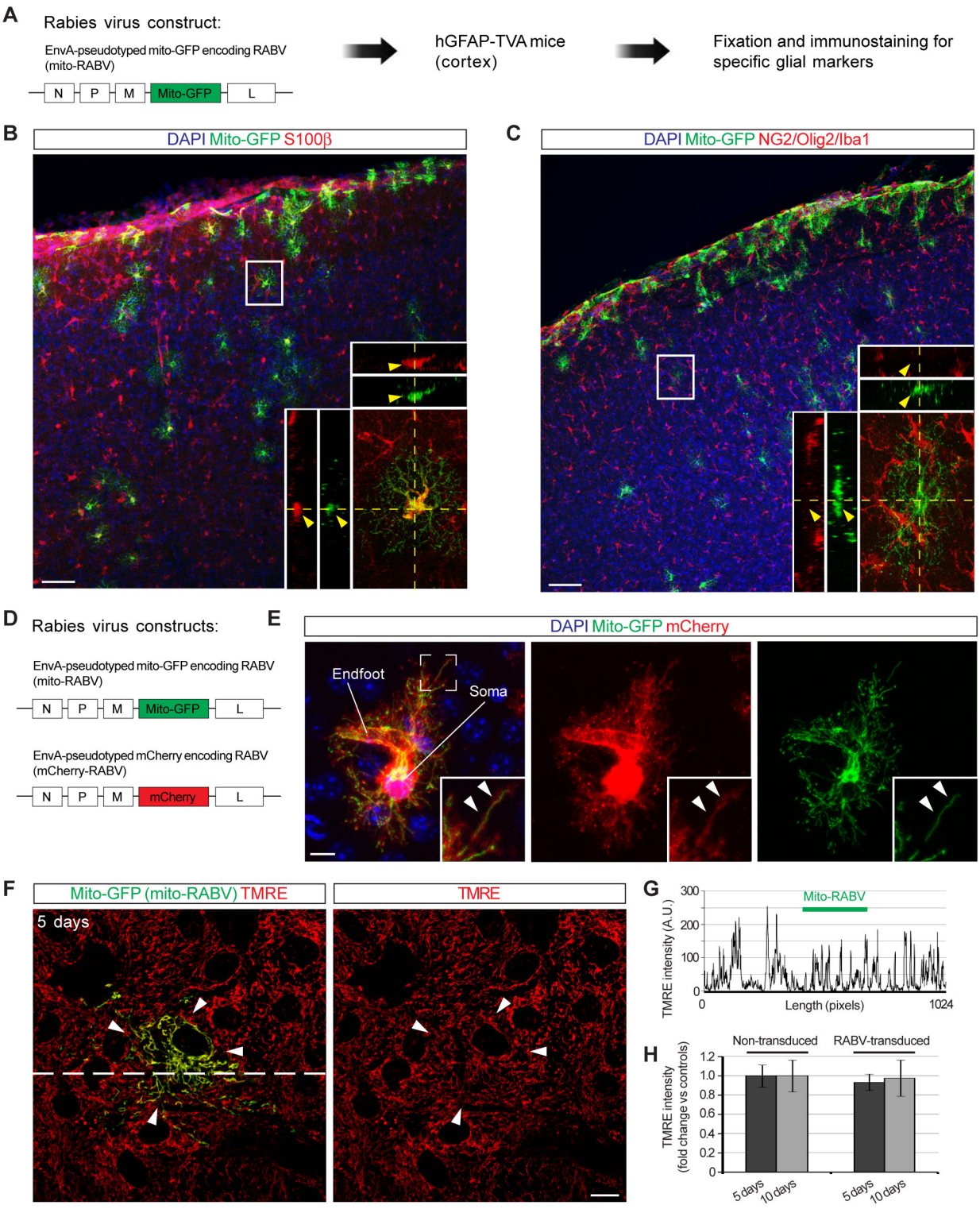
A
Rabies virus construct:
EnvA-pseudotyped mito-GFP encoding RABV (mito-RABV)
N P M Mito-GFP L
hGFAP-TVA mice (cortex)
Fixation and immunostaining for specific glial markers
B
DAPI Mito-GFP S100β
C
DAPI Mito-GFP NG2/Olig2/Iba1
D
Rabies virus constructs:
EnvA-pseudotyped mito-GFP encoding RABV (mito-RABV)
N P M Mito-GFP L
EnvA-pseudotyped mCherry encoding RABV (mCherry-RABV)
N P M mCherry L
E
DAPI Mito-GFP mCherry
Endfoot
Soma
F
Mito-GFP (mito-RABV) TMRE
TMRE
5 days
G
Mito-RABV
TMRE intensity (A.U.)
300
200
100
0
0
Length (pixels)
1024
H
Non-transduced
RABV-transduced
TMRE intensity (fold change vs controls)
1.2
1.0
0.8
0.6
0.4
0.2
0
5 days
10 days
5 days
10 days

Figure S1

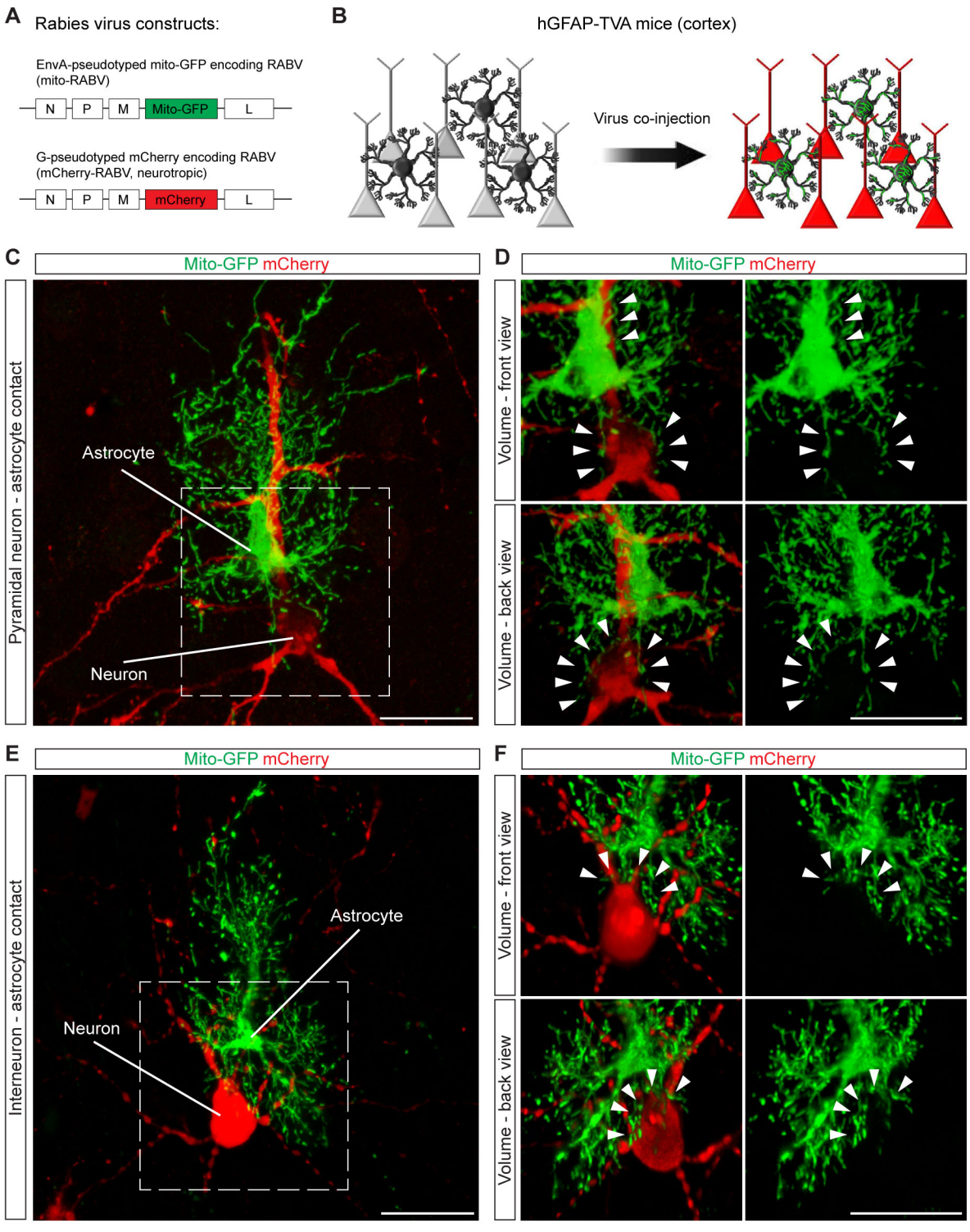
A
Rabies virus constructs:
EnvA-pseudotyped mito-GFP encoding RABV
(mito-RABV)
N
P
M
Mito-GFP
L
G-pseudotyped mCherry encoding RABV
(mCherry-RABV, neurotropic)
N
P
M
mCherry
L
B
hGFAP-TVA mice (cortex)
Virus co-injection
C
Mito-GFP mCherry
Pyramidal neuron - astrocyte contact
Astrocyte
Neuron
D
Mito-GFP mCherry
Volume - front view
Volume - back view
E
Mito-GFP mCherry
Interneuron - astrocyte contact
Astrocyte
Neuron
F
Mito-GFP mCherry
Volume - front view
Volume - back view

Figure S2

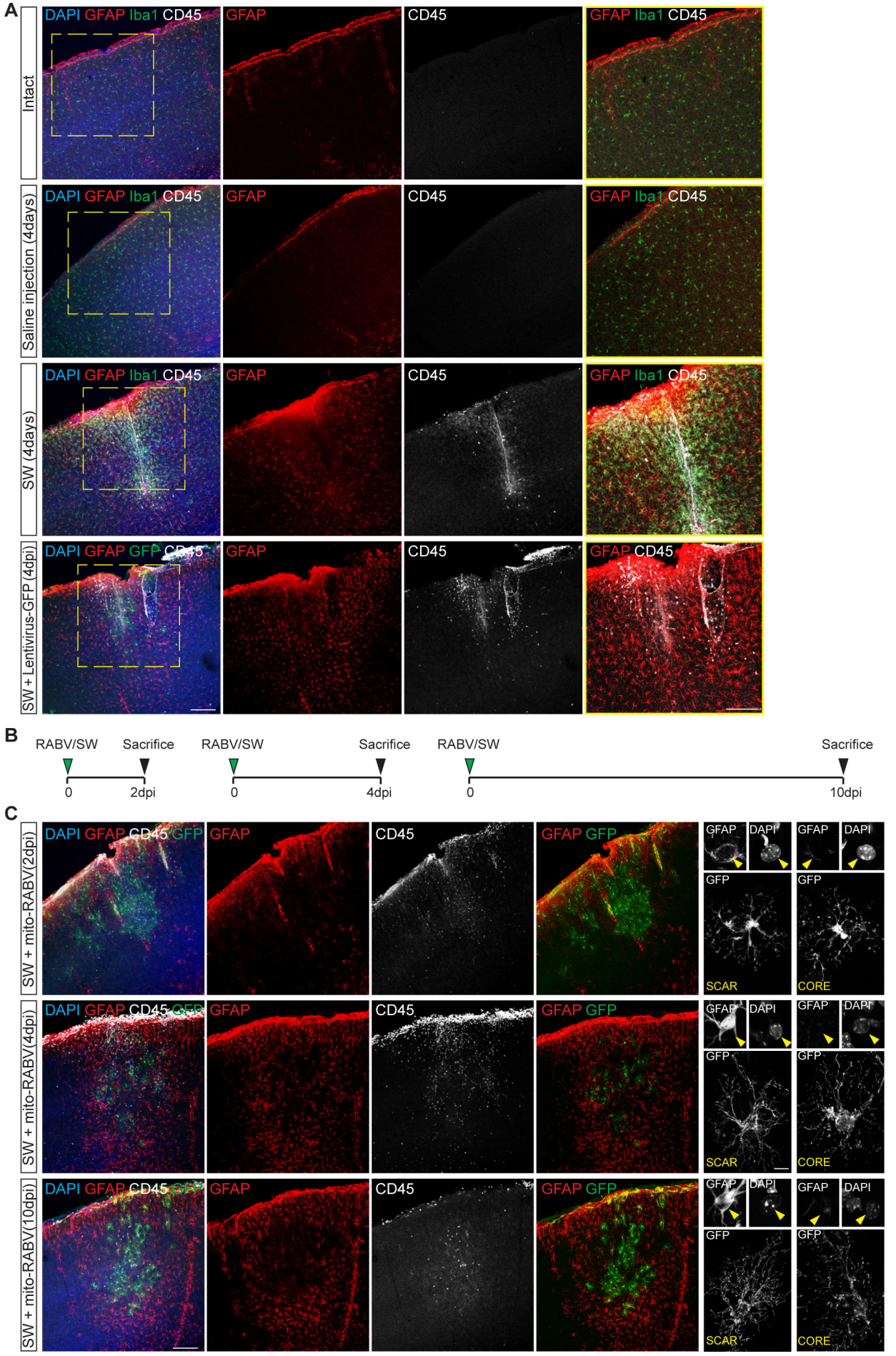
A
Intact
Saline injection (4days)
SW (4days)
SW + Lentivirus-GFP (4dpi)
DAPI GFAP Iba1 CD45
GFAP
CD45
GFAP Iba1 CD45
DAPI GFAP GFP CD45
GFAP CD45
B
RABV/SW
Sacrifice
0
2dpi
4dpi
10dpi
C
SW + mito-RABV(2dpi)
SW + mito-RABV(4dpi)
SW + mito-RABV(10dpi)
DAPI GFAP CD45 GFP
GFAP GFP
GFAP
DAPI
GFP
SCAR
CORE

Figure S3

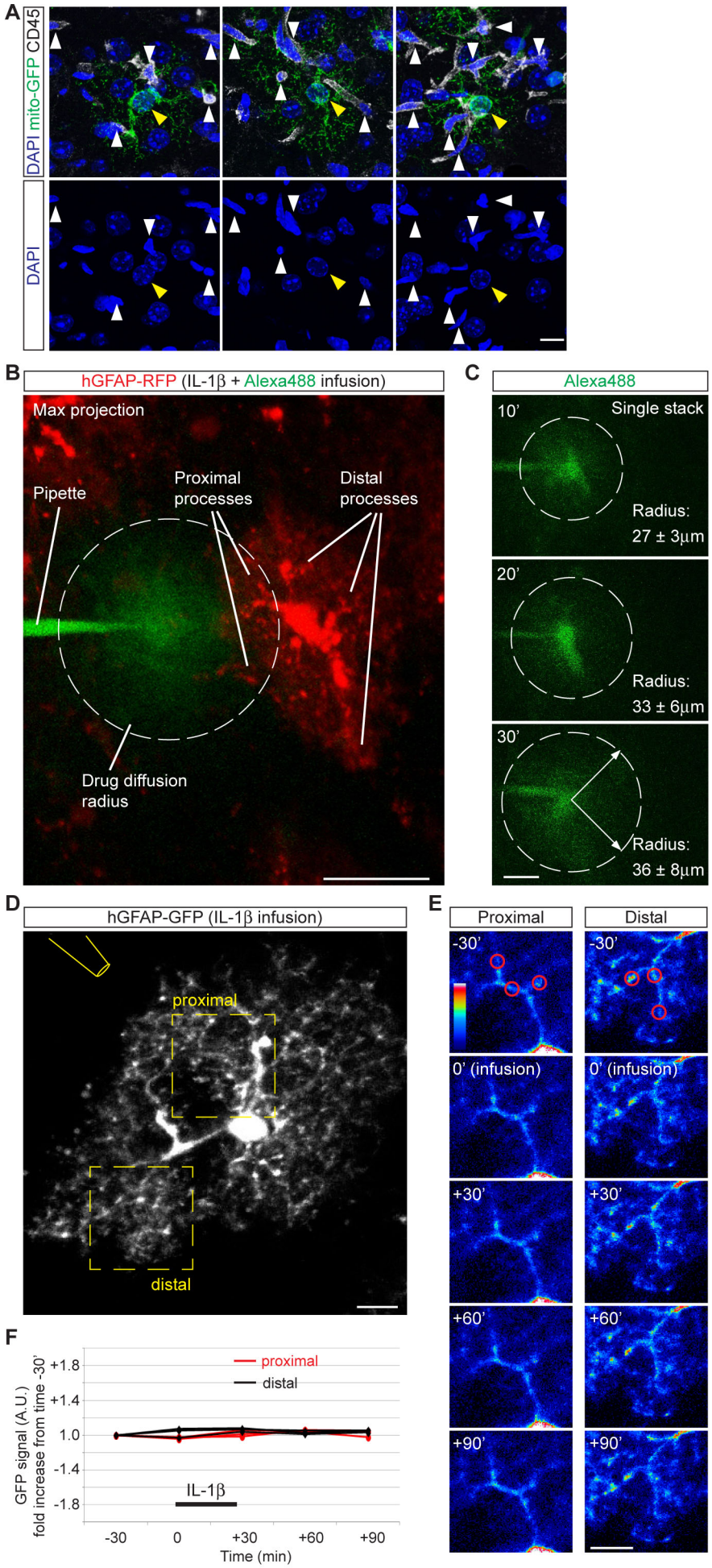
A
DAPI mito-GFP CD45
DAPI
B
hGFAP-RFP (IL-1β + Alexa488 infusion)
Max projection
Pipette
Proximal processes
Distal processes
Drug diffusion radius
C
Alexa488
10'
Single stack
Radius: 27 ± 3μm
20'
Radius: 33 ± 6μm
30'
Radius: 36 ± 8μm
D
hGFAP-GFP (IL-1β infusion)
proximal
distal
E
Proximal
Distal
-30'
0' (infusion)
+30'
+60'
+90'
F
proximal
distal
GFP signal (A.U.) fold increase from time -30'
+1.8
+1.4
1.0
-1.4
-1.8
IL-1β
-30
0
+30
+60
+90
Time (min)

Figure S4

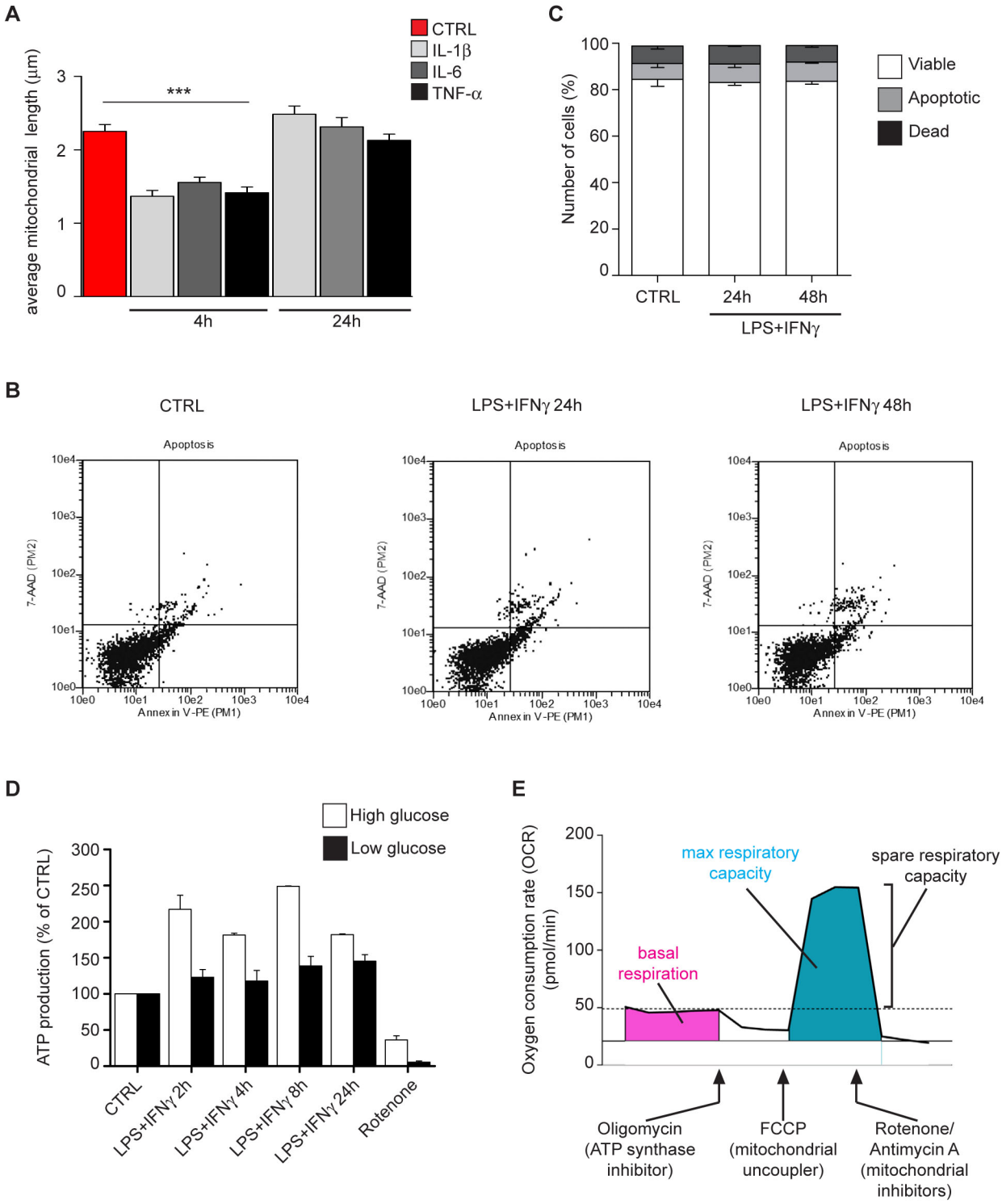
A
CTRL
IL-1β
IL-6
TNF-α
average mitochondrial length (μm)
***
4h
24h
C
Viable
Apoptotic
Dead
Number of cells (%)
CTRL
24h
48h
LPS+IFNγ
B
CTRL
LPS+IFNγ 24h
LPS+IFNγ 48h
Apoptosis
7-AAD (PM2)
Annexin V-PE (PM1)
D
High glucose
Low glucose
ATP production (% of CTRL)
CTRL
LPS+IFNγ 2h
LPS+IFNγ 4h
LPS+IFNγ 8h
LPS+IFNγ 24h
Rotenone
E
Oxygen consumption rate (OCR) (pmol/min)
max respiratory capacity
spare respiratory capacity
basal respiration
Oligomycin (ATP synthase inhibitor)
FCCP (mitochondrial uncoupler)
Rotenone/ Antimycin A (mitochondrial inhibitors)

Figure S5

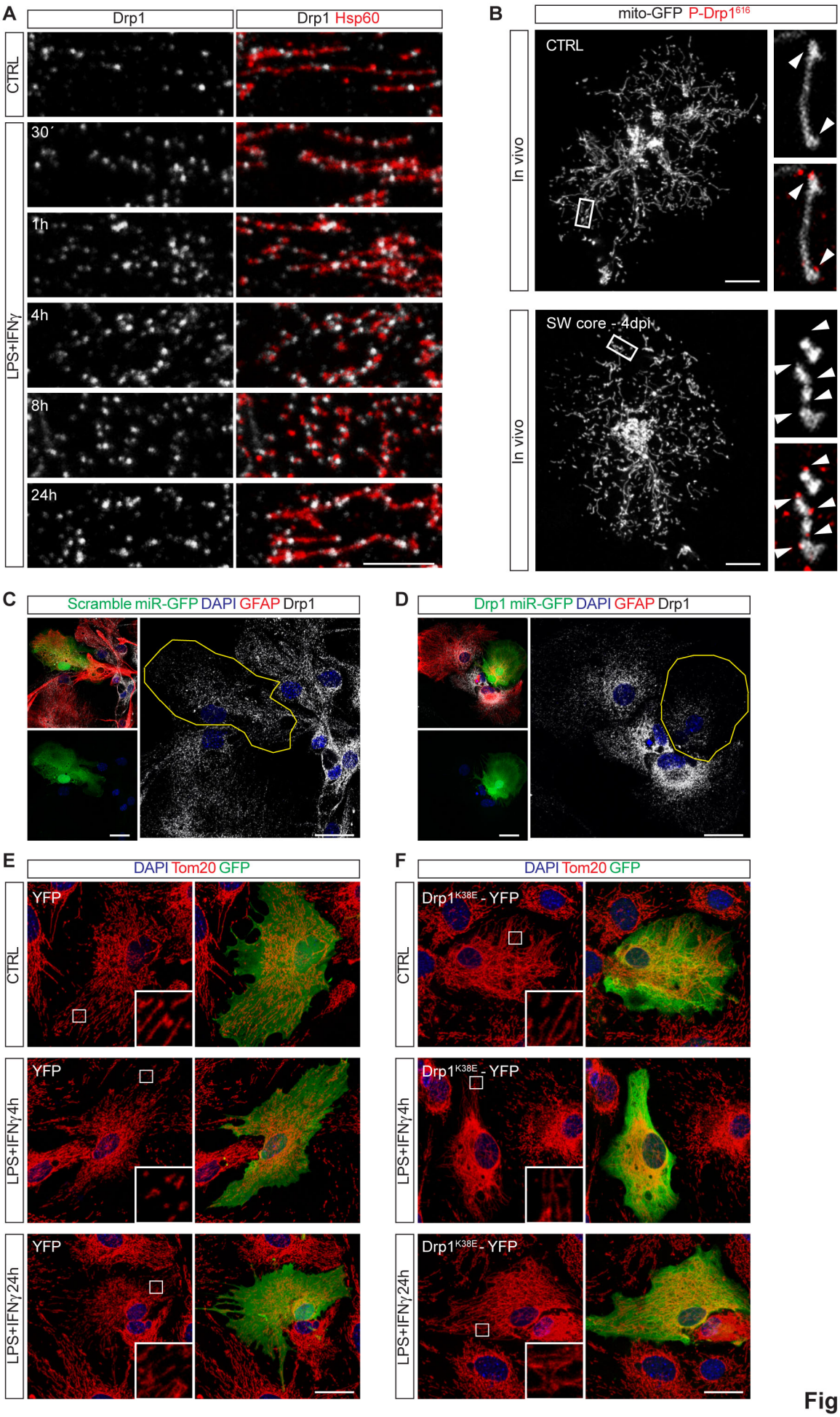
A
Drp1
Drp1 Hsp60
CTRL
LPS+IFNγ
30´
1h
4h
8h
24h
B
mito-GFP P-Drp1616
CTRL
In vivo
SW core - 4dpi
In vivo
C
Scramble miR-GFP DAPI GFAP Drp1
D
Drp1 miR-GFP DAPI GFAP Drp1
E
DAPI Tom20 GFP
CTRL
YFP
LPS+IFNγ4h
YFP
LPS+IFNγ24h
YFP
F
DAPI Tom20 GFP
CTRL
Drp1K38E - YFP
LPS+IFNγ4h
Drp1K38E - YFP
LPS+IFNγ24h
Drp1K38E - YFP

Figure S6

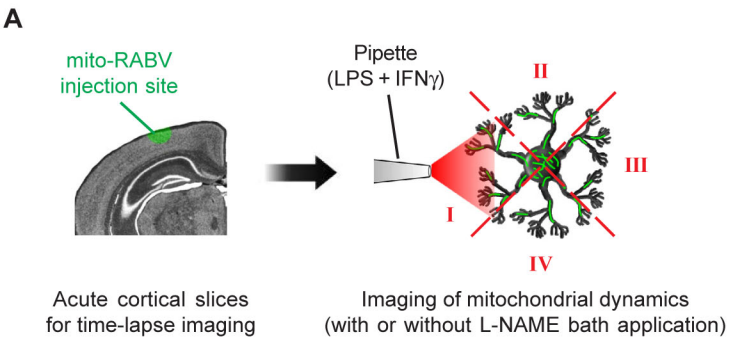
A
mito-RABV
injection site
Pipette
(LPS + IFNγ)
II
III
I
IV
Acute cortical slices
for time-lapse imaging
Imaging of mitochondrial dynamics
(with or without L-NAME bath application)

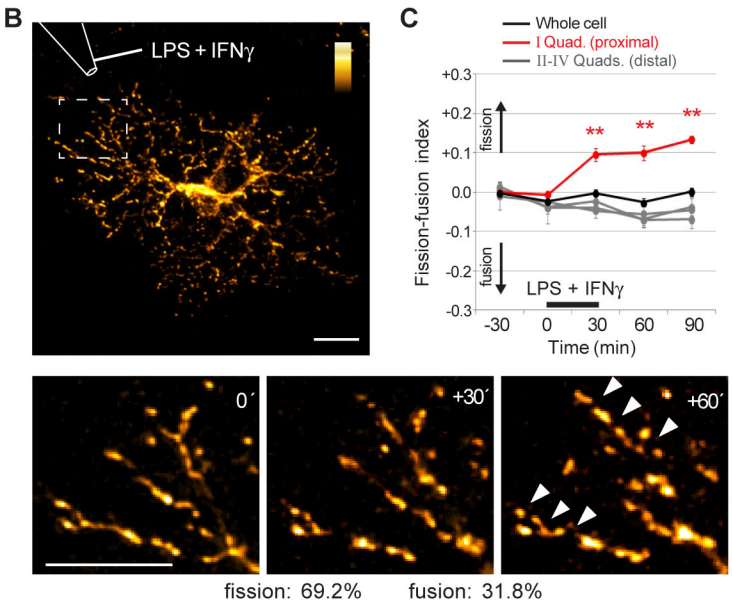
B
LPS + IFNγ
C
Whole cell
I Quad. (proximal)
II-IV Quads. (distal)
Fission-fusion index
fission
fusion
LPS + IFNγ
Time (min)
0´
+30´
+60´
fission: 69.2%
fusion: 31.8%

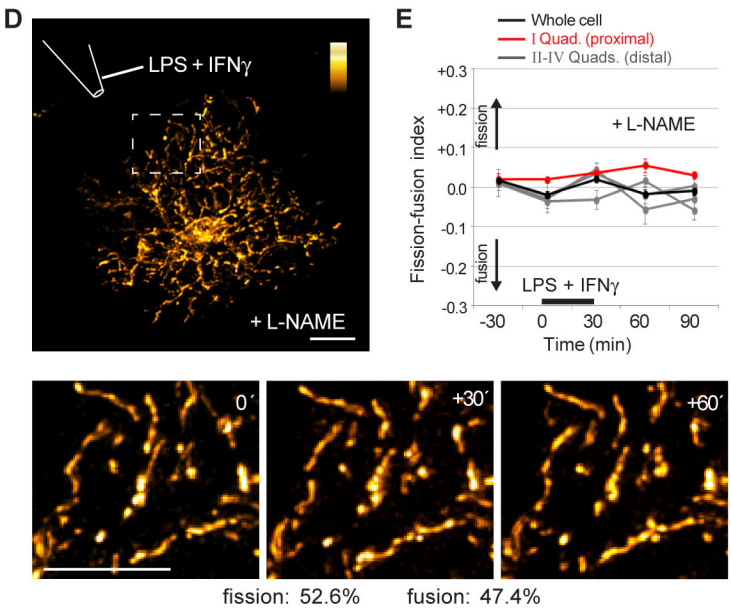
D
LPS + IFNγ
+ L-NAME
E
Whole cell
I Quad. (proximal)
II-IV Quads. (distal)
Fission-fusion index
fission
fusion
+ L-NAME
LPS + IFNγ
Time (min)
0´
+30´
+60´
fission: 52.6%
fusion: 47.4%

Figure S7

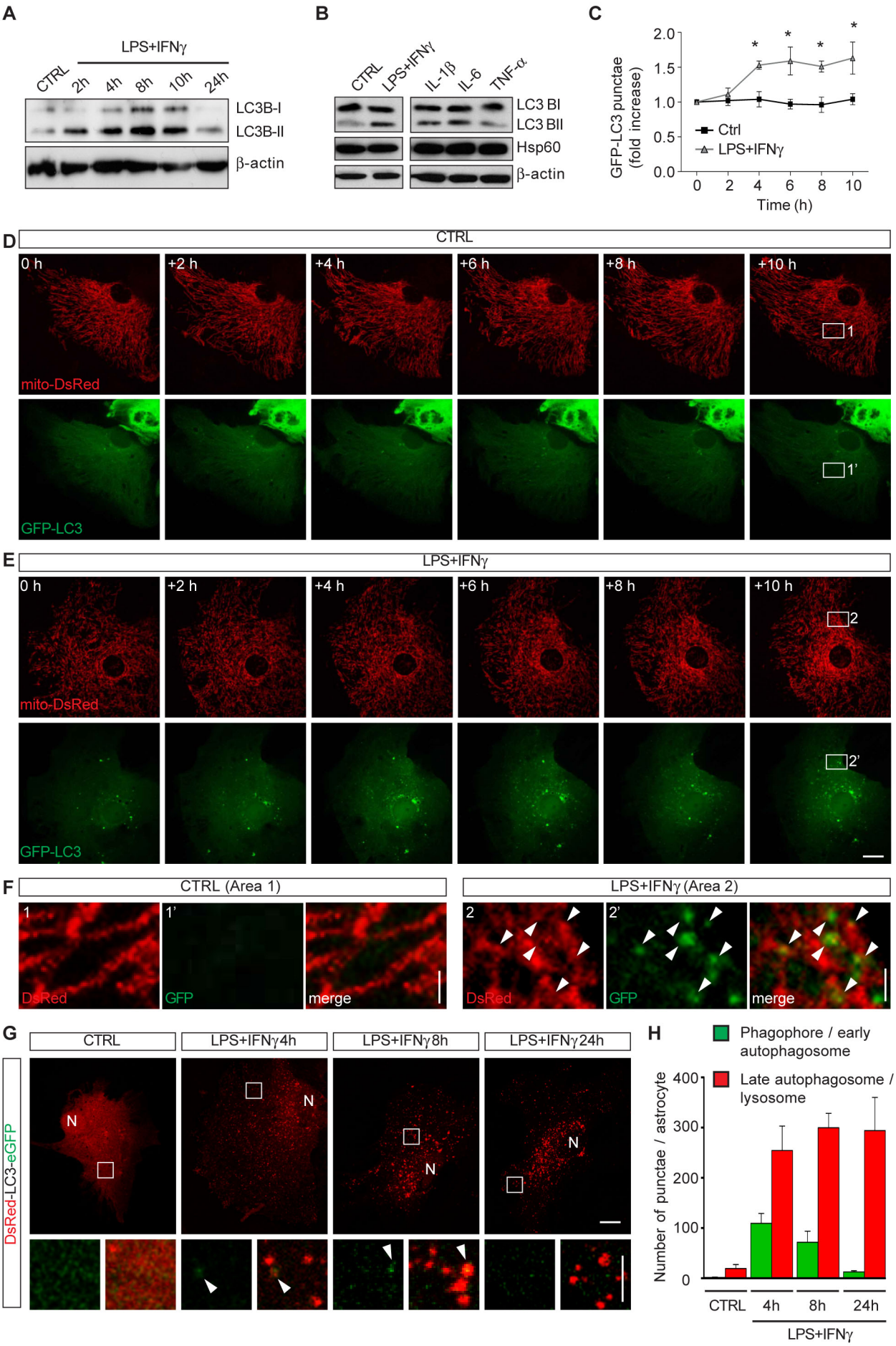
A
LPS+IFNγ
CTRL
2h
4h
8h
10h
24h
LC3B-I
LC3B-II
β-actin
B
CTRL
LPS+IFNγ
IL-1β
IL-6
TNF-α
LC3 BI
LC3 BII
Hsp60
β-actin
C
GFP-LC3 punctae (fold increase)
Ctrl
LPS+IFNγ
Time (h)
D
CTRL
0 h
+2 h
+4 h
+6 h
+8 h
+10 h
mito-DsRed
GFP-LC3
1
1'
E
LPS+IFNγ
2
2'
F
CTRL (Area 1)
LPS+IFNγ (Area 2)
DsRed
GFP
merge
G
CTRL
LPS+IFNγ4h
LPS+IFNγ8h
LPS+IFNγ24h
DsRed-LC3-eGFP
N
H
Phagophore / early autophagosome
Late autophagosome / lysosome
Number of punctae / astrocyte
CTRL
4h
8h
24h
LPS+IFNγ

Figure S8

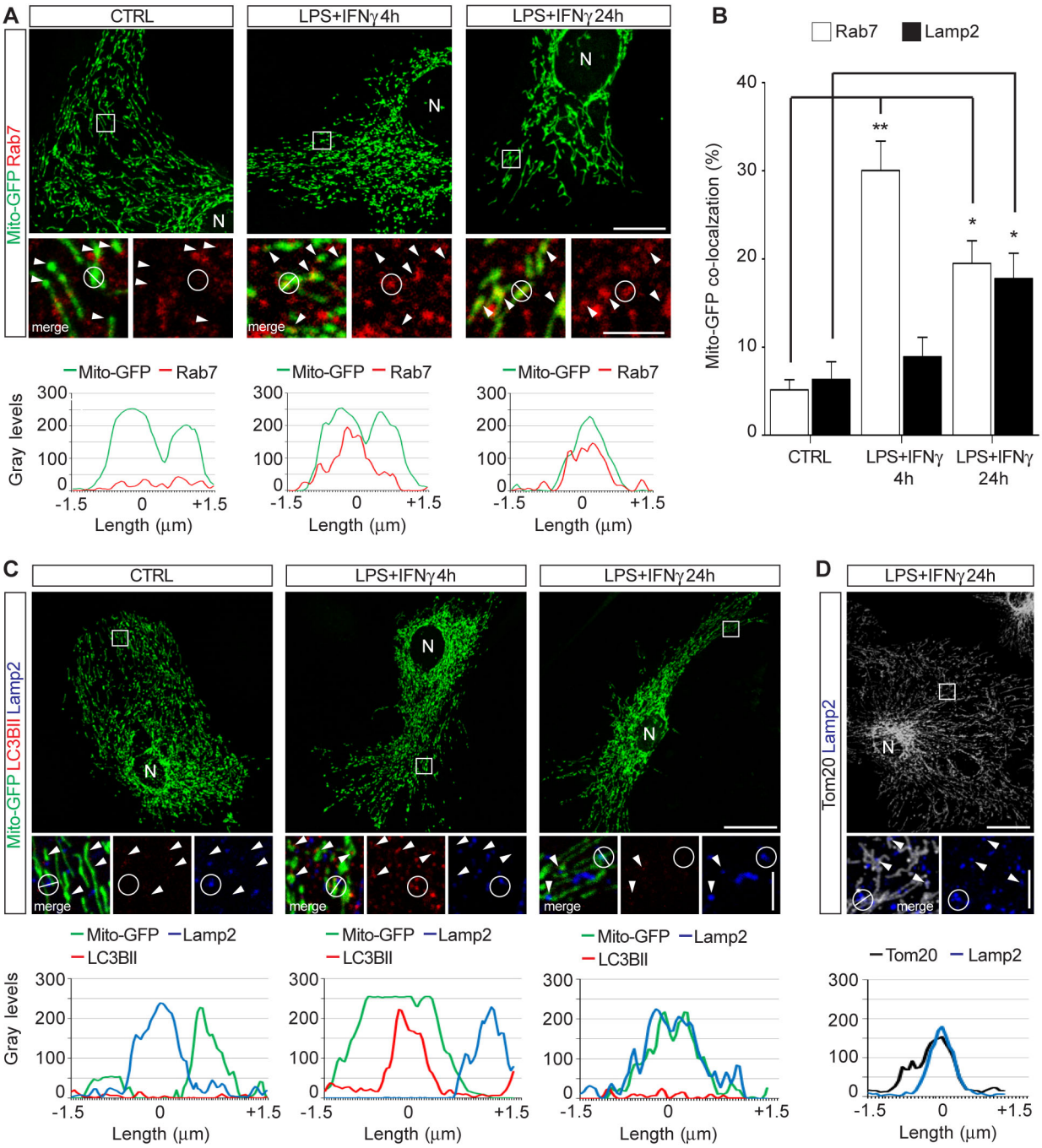
A
CTRL
LPS+IFNγ4h
LPS+IFNγ24h
Mito-GFP Rab7
N
merge
Mito-GFP
Rab7
Gray levels
300
200
100
0
-1.5
0
+1.5
Length (μm)
B
Rab7
Lamp2
Mito-GFP co-localzation (%)
40
30
20
10
0
**
*
*
CTRL
LPS+IFNγ 4h
LPS+IFNγ 24h
C
CTRL
LPS+IFNγ4h
LPS+IFNγ24h
Mito-GFP LC3BII Lamp2
N
merge
Mito-GFP
Lamp2
LC3BII
Gray levels
300
200
100
0
-1.5
0
+1.5
Length (μm)
D
LPS+IFNγ24h
Tom20 Lamp2
N
merge
Tom20
Lamp2
300
200
100
0
-1.5
0
+1.5
Length (μm)

Figure S9

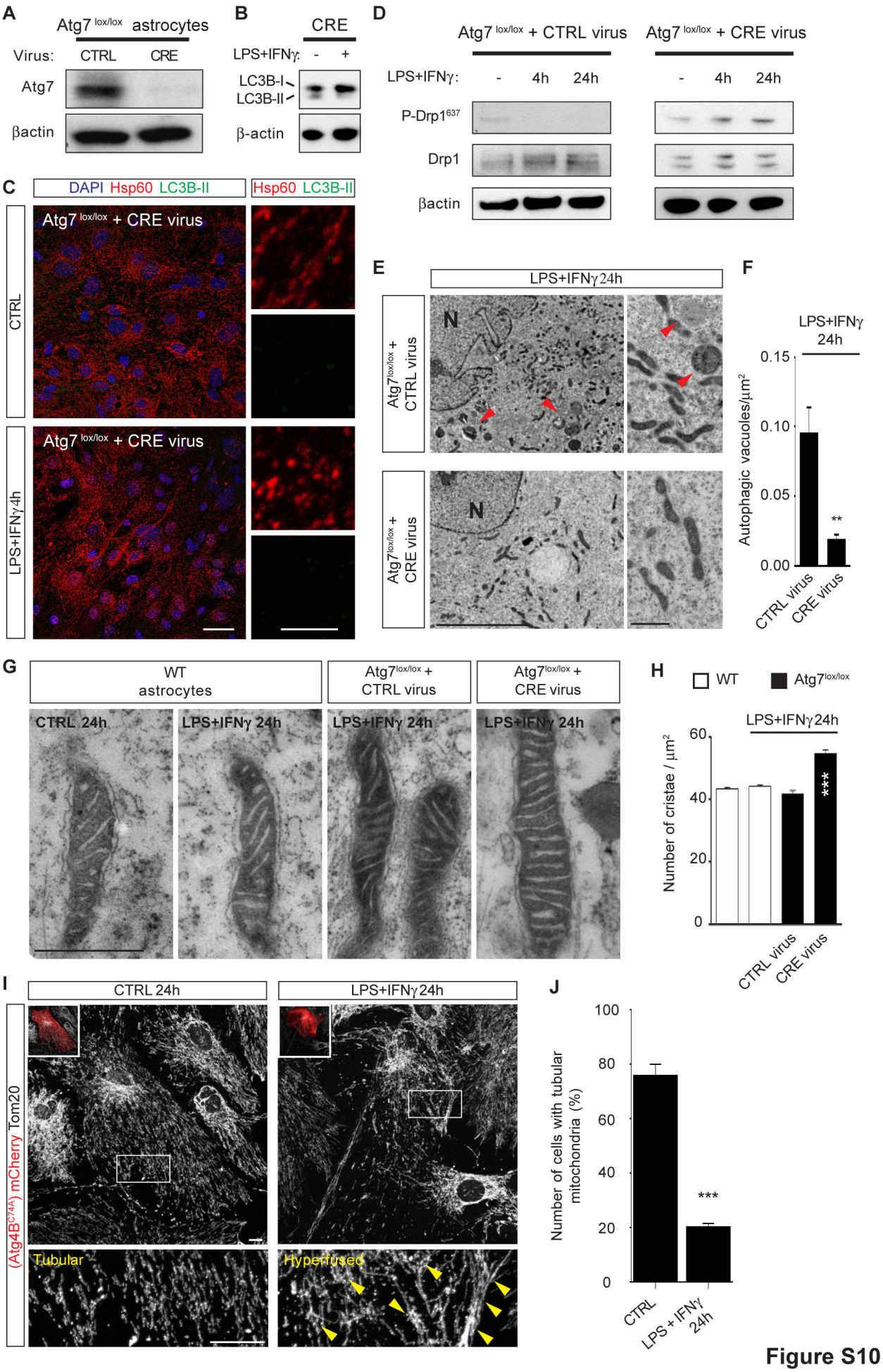
A
Atg7 lox/lox astrocytes
Virus: CTRL CRE
Atg7
βactin
B
CRE
LPS+IFNγ: - +
LC3B-I
LC3B-II
β-actin
D
Atg7 lox/lox + CTRL virus
Atg7 lox/lox + CRE virus
LPS+IFNγ: - 4h 24h
P-Drp1637
Drp1
βactin
C
DAPI Hsp60 LC3B-II
Hsp60 LC3B-II
CTRL
LPS+IFNγ4h
Atg7 lox/lox + CRE virus
E
LPS+IFNγ24h
Atg7lox/lox + CTRL virus
Atg7lox/lox + CRE virus
N
F
LPS+IFNγ 24h
Autophagic vacuoles/μm2
0.15
0.10
0.05
0.00
**
CTRL virus
CRE virus
G
WT astrocytes
Atg7lox/lox + CTRL virus
Atg7lox/lox + CRE virus
CTRL 24h
LPS+IFNγ 24h
H
WT
Atg7lox/lox
LPS+IFNγ24h
Number of cristae / μm2
60
40
20
0
***
CTRL virus
CRE virus
I
CTRL 24h
LPS+IFNγ24h
(Atg4BC74A) mCherry Tom20
Tubular
Hyperfused
J
Number of cells with tubular mitochondria (%)
100
80
60
40
20
0
***
CTRL
LPS + IFNγ 24h

Figure S10